NASA-CR-192083

Penn State
University PARK, PA
16802

GRANT
IN-47-CR
142857
P.87

Low Cloud Investigations for Project FIRE:
Island Studies of Cloud Properties, Surface Radiation, and Boundary Layer Dynamics

NAG-1-652

Principal Investigator : **Thomas P. Ackerman**
NASA Technical Officer: **Mr. Tom Owens**

Final Report
February 1, 1993

(NASA-CR-192083) LOW CLOUD INVESTIGATIONS FOR PROJECT FIRE: ISLAND STUDIES OF CLOUD PROPERTIES, SURFACE RADIATION, AND BOUNDARY LAYER DYNAMICS. A SIMULATION OF THE REFLECTIVITY OVER A STRATOCUMULUS CLOUD DECK BY THE MONTE CARLO METHOD M.S. Thesis Final Report (Pennsylvania State Univ.) 87 p
N93-18001
Unclas
G3/47 0142857

The Pennsylvania State University
The Graduate School
The Graduate Program in Meteorology

A Simulation of the Reflectivity over a Stratocumulus Cloud Deck by the Monte Carlo Method

A Thesis in
Meteorology
by

Ruei-Fong Lin

Submitted in Partial Fulfillment
of the Requirements
for the Degree of

Master of Science

May 1993

Table of Symbols

b_{abs}	Volume absorption coefficient
b_{ext}	Volume extinction coefficient
b_{scat}	Volume scattering coefficient
$\overline{d}$	Mean diameter
$F^{\downarrow}$	Downward flux
$F^{\uparrow}$	Upward flux
g	Asymmetric factor
I	Intensity (Radiance)
l	Free path
l_0	Mean free path
LWC	Liquid water content
N_d	Number density
N_{in}	Number of incident photons
$N_{out,top}$	Number of reflected photons
$p(\,)$	Probability density function
$p_c(\,)$	Cumulative probability density function
$P(\,)$	Phase function
$\overline{r}$	Mean radius
$\overline{r_g}$	Geometric mean radius
$\mathbf{r}$	Position vector
R_i	A random number between 0 and unity
$\mathrm{Re}\,f_b$	Bulk reflectivity
$\mathrm{Re}\,f_p$	Reflectivity at a point

T	Temperature
ϕ	Azimuth Angle
λ	Wavelength
θ	Latitude
Θ	Zenith Angle
ρ_w	Water density
σ	Standard deviation
σ_{ext}	Monochromatic extinction cross section
σ_g	Geometric standard deviation
τ	Optical depth
ϖ_0	Single scattering albedo
ω	Direction vector

Acknowledgment

Two and a half years have passed by; finally, I finish my requirement to get a master degree in Meteorology. In this happy moment, my thanks go to those who help me getting through this bitter-and-sweet thesis creating process.

I am most grateful to my thesis advisor, Dr. Thomas P. Ackerman. With his patient guidance, I not only learn how to do research work, but also enjoy the delight and pleasure that study brings to me. My thanks goes to Dr. Albrecht for his precious suggestions and discussions about this thesis. Gratitude goes to Dr. Thompson for his signature.

I am grateful to Qing Wang for her generous help in the FIRE data. I am thankful to Dr. Yun Han, Andy Vogelmann, and Adrian George for their discussions about this work.

Special gratitude goes to my parents and my brother. Only with their support and encouragement can I always remind myself of my motivation in research work, and struggle through the hardship. I also want to thank my good friends, you are the wind beneath my wings. As for it is geostrophic wind or ageostrophic wind, it is really beyond the scope of this thesis.

Abstract

The radiation field over a broken stratocumulus cloud deck is simulated by the Monte Carlo method. We conducted four experiments to investigate the main factor for the observed shortwave reflectivity over the FIRE flight 2 leg 5, in which reflectivity decreases almost linearly from the cloud center to cloud edge while the cloud top height and the brightness temperature remain almost constant through out the clouds. From our results, the geometry effect, however, did not contribute significantly to what has been observed. We found that the variation of the volume extinction coefficient as a function of its relative position in the cloud affects the reflectivity efficiently. Additional check of the brightness temperature of each experiment also confirms this conclusion.

The cloud microphysical data showed some interesting features. We found that the cloud droplet spectrum is nearly log-normal distributed when the clouds were solid. However, whether the shift of cloud droplet spectrum toward the larger end is not certain. The decrease of number density from cloud center to cloud edges seems to have more significant effects on the optical properties.

Chapter 1

INTRODUCTION

The recent concern about the possible effects of anthropogenic pollutants, such as CO_2, CH_4, CFC, etc., on the climate change has urged the study of feedback mechanisms within our climate system. Cloud feedback mechanisms, which include changes in cloud type, coverage, and cloud droplet size induced by the change of some other climatic factors, are among the least understood feedback mechanisms. Yet, the importance of the effects of clouds on the radiation budget has been acknowledged. The magnitude of the global shortwave, longwave and net radiative forcing are all one order greater than that of CO_2 doubling (Ramanathan et al. ,1989). This implies that small changes in the cloud radiative forcing could result in a significant alternation of the Earth's radiation budget.

From a radiation budget point of view, stratus and stratocumulus clouds have long been recognized for their importance to the climate system because of their large-area coverage and longevity. Both of the stratus and the stratocumulus clouds are typically found on the eastern rim of sub-tropical high pressure systems: for instance, the west coast of California in the summer, southern Peru, northern Chile, and south west Africa. Yet, the spatial scales of stratocumulus and stratus clouds are different: an individual stratocumulus cloud ranges around $10^2 km^2$ while the stratus deck could extend to $10^6 km^2$ in area.

However, one of the defects in all the present general circulation models (GCM) is their inability to calculate radiative transfer through the broken cloud field, which is a feature of stratocumulus clouds. Most of the GCMs assume that a homogeneous cloud deck covers the entire grid point once the grid point is saturated. It is postulated that the radiation budget over a broken cloud field would differ significantly from its homogenous counterpart.

Many efforts have been devoted to the investigation of radiative transfer through inhomogeneous clouds. Blerkom (1971) studied how the striate cloud-top structure which could result from convective motion in the stratiform clouds affects the shortwave radiation field. He found that the reflected radiance depends on both the degree of striation and the incident angle.

McKee and Cox (1974) investigated the reflected irradiance of a cubic-shaped cloud and compared it with that of horizontally semi-infinite clouds. Their analysis showed that the incident solar flux on the vertical sides of cubic clouds has a significant effect on the reflected irradiance.

Welch and Wielicki (1984) surveyed the effects of cloud shapes and cloud alignment patterns on radiation. They studied the bulk reflectivity at visible wavelengths as a function of the incident solar zenith angle and fractional area coverage for four different shapes of clouds aligned in a linear or hexagonal array. Their conclusion was that plane-parallel calculations are not satisfactory at most values of cloud cover. Hence, the importance of cloud shapes and cloud alignment patterns to the radiation field is assured.

Yet, despite the inclusion of cloud geometry effects, these previous studies assume the optical properties, especially the visible volume extinction coefficient, remain constant in clouds. However, it is conjectured that turbulent motions in stratocumulus clouds, rising motion in the cloud center and sinking motion at the cloud edge, could result in horizontal and vertical inhomogeneity of cloud microphysics properties. Thus, the volume extinction coefficient might vary horizontally and vertically in stratocumulus clouds.

Furthermore, these previous studies mainly focus on the study of bulk reflectivity. This is understandable because, from a climate point of view, it is the bulk reflectivity of clouds that relates directly to the radiation budget. Besides, no *in situ* measurements of cloud point reflectivity, which is defined as the upward flux at a point above the cloud dividing by its associated downward flux, were available then.

The Marine Stratocumulus Intensive Field Observations (IFO) phase of the First International Satellite Cloud Climatology Project Regional Experiment (FIRE) in the summer of 1987 collected precise and interesting data of stratocumulus clouds. Among these data, we are primarily interested in the change of the cloud point reflectivity along the flight path detected by the NCAR Electra on June 30. The cloud point reflectivity changes drastically from cloud edges to cloud centers in a wave-like form with troughs at cloud edges and ridges at cloud centers. In contrast, the cloud-top height remains almost constant except a sharp decrease of height at cloud edges.

We can not help but ask the question: is this a result of the shape of the cloud? Or are some other factors associated with this phenomenon? Note, that here the bulk reflectivity is not the concern, but rather the cloud point reflectivity as a function in space.

The Monte Carlo method is the only known computational method capable of simulating radiative transfer through media in which complicated inhomogeneity is present. The reason is that, unlike the other computational methods for atmospheric optics, the Monte Carlo method simulates the radiation field by tracking photons, which gives the Monte Carlo method flexibility in dealing with complicated inhomogeneity in the media. Thus, for cases like simulating the cloud point reflectivity over broken cloud field with the change of cloud optical properties considered, the Monte Carlo method is indeed the only choice. As a matter of fact, it terms out that tracking photons is the easy part of the simulation whereas specifying the inhomogeneity of the cloud field and discussing the statistics of results are more challenging.

Chapter 2 briefly describes the basic concepts and the equation of radiative transfer in atmospheric science. The theory, procedures, and statistics of the Monte Carlo method are also illustrated for their application to simulations of the radiation field of both homogeneous and inhomogeneous clouds.

Chapter 3 introduces the instruments used in the IFO phase of FIRE, and also the general cloud conditions when the data was collected. Some basic arithmetical calculations implied in the data are shown. The data of the cloud microphysics properties and the cloud radiative filed are discussed.

Chapter 4, first of all, briefly describes important concepts about the Mie scattering code, the hemispheric mean technique, and the flux extrapolation scheme. These three techniques help the fulfillment of our simulations of the cloud radiation field and the comparisons between simulation results and observational data. Second, it lists all the constants and variables in the simulations. Detailed display and discussions of our simulation results are then demonstrated. A concise conclusion of this study is presented in Chapter 5.

Chapter 2

Computation Method

In the field of atmospheric radiation, the equation of transfer, which can be solved analytically only in some special cases, is noted for its mathematical complexity. Thus, efforts have been made on the development of computational procedures.

Among these techniques, the Monte Carlo method is most capable of simulating the radiative field of horizontally inhomogeneous clouds, especially when the cloud geometry and the horizontal variation of the volume extinction coefficient are both considered. Therefore, the Monte Carlo method is employed to simulate the radiation field of stratocumulus clouds in this study. Chapter 2 will briefly review the basic concepts of the equation of transfer, and the theory, procedure, and statistics of the Monte Carlo method.

2.1 The Equation of Transfer

Intensity (radiance), in units of energy per area per time per frequency and per steradian, is a basic radiometric quantity in the radiative transfer process. Even though intensity is a scalar, a directionality is implied in its definition. Figure (2.1) is a schematic diagram of the vectors related to intensity. $I_\lambda(\mathbf{r},\omega)$ denotes the intensity of a pencil of light at position **r** with a wavelength λ pointing with a direction ω (ω is an unit vector) at point A. However, as the pencil of light passes through the medium from A to B, its intensity changes to $I_\lambda(\mathbf{r}+d\mathbf{r},\omega)$, where $d\mathbf{r} = \omega ds$ and ds is the infinitesimal distance between point A and point B..

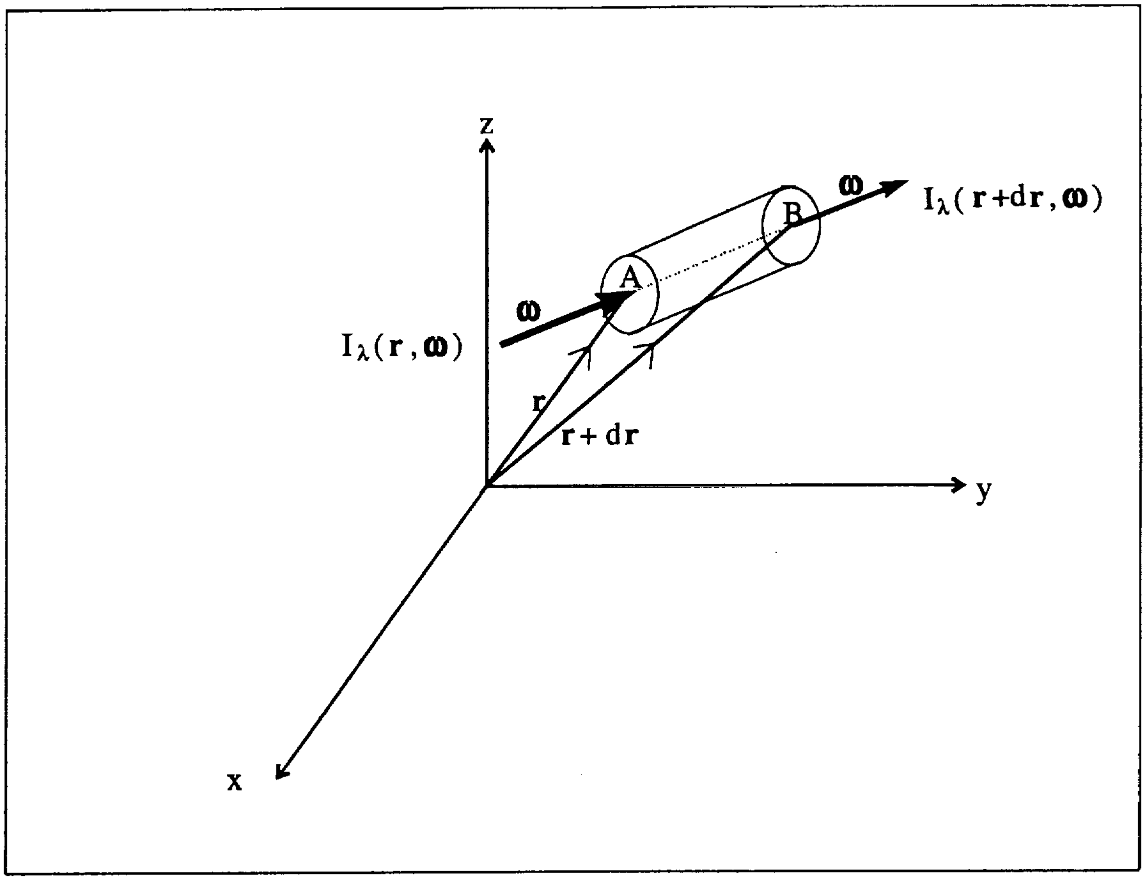

Figure (2.1) A schematic diagram for a beam of light, intensity $I_\lambda(\mathbf{r},\omega)$ at point A, passes through a medium from point A to point B and its associated directionality in an arbitrary 3-dimensional coordinate.

Compare the intensity at point A with the intensity at point B. One will find out that the difference between $I_\lambda(\mathbf{r}+d\mathbf{r},\omega)$ and $I_\lambda(\mathbf{r},\omega)$,

$$\mathbf{dI}_\lambda(\mathrm{r},\omega)=\mathbf{I}_\lambda(\mathrm{r}+\mathbf{d}\,\mathrm{r},\omega)-\mathbf{I}_\lambda(\mathrm{r},\omega) \qquad (2.1),$$

is a result of loss and gain of intensity from three different mechanisms.

As the light beam originally with a value $I_\lambda(\mathbf{r},\omega)$ traverses through the medium from A to B, it is attenuated because a portion of the light beam is absorbed or scattered out into another direction by the medium. The monochromatic volume extinction coefficient $b_{ext,\lambda}(\mathbf{r})$, which is the sum of the monochromatic volume scattering coefficient $b_{scat,\lambda}(\mathbf{r})$ and the monochromatic volume absorption coefficient $b_{abs,\lambda}(\mathbf{r})$, characterizes the amount of attenuation. Note $b_{ext,\lambda}(\mathbf{r})$, $b_{scat,\lambda}(\mathbf{r})$, and $b_{abs,\lambda}(\mathbf{r})$ are all in units of per length. The single scattering albedo ϖ_0 is defined as $\frac{b_{scat,\lambda}(\mathbf{r})}{b_{ext,\lambda}(\mathbf{r})}$. Hence, if only the loss term is considered,

$$dI_\lambda(\mathbf{r},\omega) = -b_{ext,\lambda}(\mathrm{r})I_\lambda(\mathbf{r},\omega)ds \qquad (2.2).$$

The gain mechanisms add complexity to this problem. We will introduce the concept of a light beam as a packet of photons in order to simplify our discussion.

In 1905, Einstein proposed the photon theory: basically, energy of electromagnetic wave behaves as if it is concentrated in photons instead of spreading out uniformly over the wave fronts. Based on this theory, a beam of light can be seen as a packet of photons. Apply this notion to radiative transfer, the interaction between the electromagnetic wave with media which the wave passes through becomes photons colliding with particles of the media.

Previously, ds is denoted mathematically as a scalar with an infinitesimal value. From a physical point of view, we can define ds as a distance much shorter than that of the mean free path of collisions between photons and particles of the medium. Thus, within ds, the probability that more than one collision takes place is very small. Then we can simplify our discussion about multiple scattering which occurs within the path ds.

First, photons which before the collision with particles of the medium propagate in the direction ω' could be scattered into ω after the collision. $P(\mathbf{r},\omega',\omega)$, the phase function, is the probability of this event. Note the phase function is also a function of position. Therefore, within ds, this gain of intensity in direction ω can be expressed as $b_{scat}\int I_\lambda(\mathbf{r},\omega')\, P(\mathbf{r},\omega',\omega)d\omega'$.

Second, emission of light by the particles in the medium could also contribute to the gain of intensity. This term could be written as $\Phi(\lambda,\mathbf{r},\omega)$.

Combine the three mechanisms above, we can write the equation of transfer as:

$$\omega\cdot\mathbf{grad}\; I_\lambda(\mathbf{r},\omega) = -b_{ext,\lambda}(\mathbf{r})I_\lambda(\mathbf{r},\omega)ds + b_{scat,\lambda}(\mathbf{r})\int_0^{2\pi} I_\lambda(\mathbf{r},\omega')\, P(\mathbf{r},\omega',\omega)d\omega'$$

$$+ \Phi(\lambda,\mathbf{r},\omega) \quad (2.3)$$

For homogeneous media, in which $b_{ext,l}$, $b_{scat,l}$, P and Φ are not functions of $\mathbf{r}$, Equation (2.3) may be solved analytically. However, solving this integral-differential equation analytically thus to obtain the radiation field is almost impossible for inhomogeneous media. Therefore, many efforts have been devoted to solving the equation computationally. However, most of the computational procedures are limited to the plane-parallel atmosphere approximation, in which all the variables in equation (2.3) only varies with height.

Horizontal homogeneity might be a good assumption for the simulation of the radiation field of stratus, which often covers area of 10^6 km^2. However, this assumption is not suitable for stratocumulus clouds, in which cell structures are often observed. The next section elaborates on the theory, procedure and statistics of Monte Carlo method and explains how it simulates the radiation field of stratocumulus clouds.

2.2 The Monte Carlo Method for An Infinite, Homogeneous, Non-Absorbing Cloud Deck

Instead of solving the equation of transfer directly, the Monte Carlo method approaches the problem of radiative transfer by modeling stochastic collisions between photons and particles. By direct simulation of photon trajectories in the cloud, the reflectivity or transmissivity of the cloud becomes one of determining what percent of the incident photons are reflected or transmitted under the premise that a sufficient number of incident photons has been input.

For simulating an infinite, homogeneous, non-absorbing cloud deck, in which the monochromatic volume extinction coefficient (abbreviated as the extinction coefficient in the following text), phase function are constant through out the whole cloud deck, the Monte Carlo method could be less efficient than other computational method because it costs computer time for optically thick clouds. Nevertheless, a close look at the way how the Monte Carlo method simulates light going through an infinite homogeneous cloud deck provides insight to the method. The theory, computational algorithm and statistics are discussed in the following sub-sections.

2.2.1 Theory

The Monte Carlo method takes full advantages of the photon theory in solving the problem of radiative transfer. Since a beam of light behaves like a packet of photons, we can simulate photon collision processes, namely, photons colliding with cloud droplets in this case, and obtain the radiation field. The whole simulation is only a photon tracing scheme in which only simple geometric computations are necessary. The idea of the Monte Carlo method is straight forward; however, in order to simulate collision processes faithfully, specifying the optical properties of cloud droplets becomes decisive to simulation results. The optical properties necessary to be specified for a non-absorbing cloud deck, in which the single scattering albedo is equal to 1, are the mean free path, the probability density function for the free path, the asymmetry factor, and the probability density function for the scattering angle.

l_0, the mean free path of collisions between a photon and a cloud droplet, is defined as $1 / b_{ext,\lambda}$. $b_{ext,\lambda}$ stands for the extinction coefficient, which is the integral of the volume extinction cross section of all cloud droplets over a unit volume. In another word, when paving all the cloud droplets of a unit volume onto a unit surface, $b_{ext,\lambda}$ equals the ratio of integral of cross section to the unit area. Thus, the inverse of $b_{ext,\lambda}$, stands for the height of a unit-area-based volume for which the integral of cross section is equal to one unit area. Hence, as a mean, when a photon travels downward from the top of this volume, it will collide with one cloud droplet before the photon leaves the volume. That is why l_0 is defined as such.

The Poisson process suits to describe collisions between a single photon and cloud droplets, because these collisions possess the necessary and sufficient properties of the Poisson process. (1.) They don't have memory to previous collision events. (2.) The probability that a single collision would occur in a small region is proportional to the size of the region and does not depend on the number of collisions outside this region. (3.) The probability that more than one collision would take place in such a small region is negligible.

The probability distribution of the Poisson random variable x, representing the number of outcomes occurring in a given interval or a specified region denoted by t, is given by

$$p(x,\nu t)=\frac{(\nu t)^{x}\exp(-\nu t)}{x!}, \qquad x=0,1,2,\ldots \qquad (2.4),$$

where ν may be interpreted as the mean number of events per unit time or per unit volume. Applying this formula to collision processes, we will get equation (2.5)

$$p(x,\frac{t}{l_0})=\frac{(\frac{t}{l_0})^{x}\exp(-\frac{t}{l_0})}{x!}, \qquad x=0,1,2,\ldots \qquad (2.5),$$

in which x is the number of collisions within the region, t is the size of an a region.

The free path l is defines as the distance between two successive collisions. For an arbitrary distance t, the probability that the free path l exceeds t, $p_c(l>t)$, equals the probability that no collisions occur within t, $p_c(l>t)=p(0,\frac{t}{l_0})=\exp(-\frac{t}{l_0})$. Therefore, the cumulative distribution function $p_c(0\le l\le t)$ becomes

$$p_c(0\le l\le t) = 1-p_c(l>t) = 1-\exp(-\frac{t}{l_0}) \qquad (2.6).$$

We may differentiate equation (2.6) with respect to t to obtain the probability density function for free path:

$$p(l)=\frac{1}{l_0}\exp(-\frac{l}{l_0}) \qquad (2.7)$$

The asymmetry factor is defined as $g = \overline{\cos\Theta} = \frac{1}{4\pi}\int_0^{2\pi}\int_0^{\pi} P(\cos\Theta)\cos\Theta\sin\Theta\, d\Theta\, d\phi$, where $P(\cos\Theta)$ is the phase function and Θ is the zenith angle and ϕ is the azimuth angle of the scattering vector (Θ,ϕ). The scattering vector is defined relative to the direction in which the photon propagates before a collision. Θ is between 0 and $\pi/2$ for forward scattering, between $\pi/2$ and π for backward scattering. ϕ is 0 when the scattering vector points at the positive x direction of our arbitrarily defined (x,y,z) coordinate, and ϕ increases counterclockwise to 2π.

The Henyey-Greenstein phase function is used in this research:

$$P(\cos\Theta) = (1 - g^2) / (1 + g^2 - 2g\cos\Theta)^{3/2} \qquad (2.8)$$

2.2.2 Computational Procedure

Figure (2.2) is the flow chart of the procedure of the Monte Carlo method for an infinite, homogeneous, and non-absorbing cloud deck. From the chart, the essence of the Monte Carlo method is no more than tracking incident photons. The only condition is that we must know g, l_0, ϖ_0 first in order to proceed tracking.

ϖ_0 determines the probability that a photon is absorbed or scattered when it collides with a cloud droplet. For visible radiation through clean water clouds, $\varpi_0 \approx 0.9999$. Thus, for optically thin water clouds, $\varpi_0 = 1$ is a good approximation.

From the previous section, we know that the probability density function for the free path, l, is an exponential distribution (see equation (2.7)). Since the integral of equation (2.7) from $l = 0$ to $l \to \infty$ is equal to 1, we can define a one-to-one relation for a random number $R_{i,l}$, whose value is uniformly distributed between zero and unity, and a free path as follows:

$$l = l_0 \ln(1 / R_{i,l}) \qquad (2.9).$$

In other words,

$$R_{i,l} = \int_{l' \to 0}^{l' \to \infty} \frac{1}{l_0} \exp(-\frac{l'}{l_0}) dl' \qquad (2.10).$$

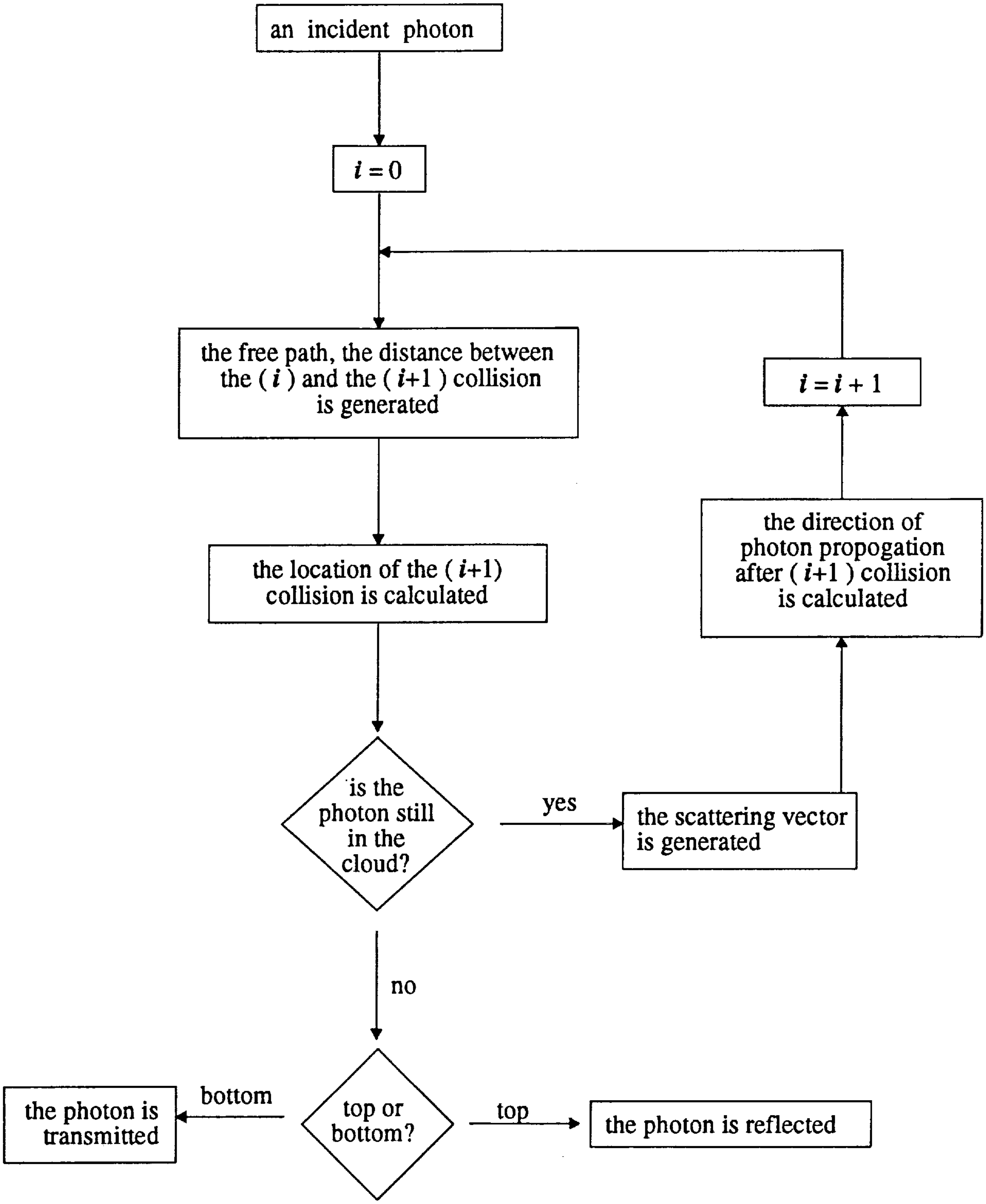

Figure (2.2) The flow chart for simulating the reflectivity and transmissivity for a infinite, homogeneous, non-absorbing cloud deck. g, l_0, ϖ_0, and $b_{ext,\lambda}$ are known.

Free paths are thus generated by the use of equation (2.9).

The phase function, which is the probability density function for the scattering process ($\frac{1}{4\pi}\int_0^{2\pi}\int_0^{\pi} P(\cos\Theta)\sin\Theta \, d\Theta \, d\phi = 1$), is then divided into 1000 equal probability bins. Each bin has the same area in the probability density function versus solid angle diagram. For each bin, we can define a mean angle Θ_m:

$$\Theta_m = \cos^{-1}\{\frac{1}{2}\,[\cos\Theta_{(\text{at the left margin of the bin})} + \cos\Theta_{(\text{at the right margin of the bin})}]\} \qquad (2.11).$$

Thus, when a bin is randomly picked up, Θ_m corresponded to the bin is set to be the Θ angle of the scattering vector. ϕ is much easier to obtain: $\phi = 2\,\pi\,R_{i,\phi}$, where $R_{i,\phi}$ is a random number between zero and unity.

By tracking photons, we then can count the number of photons that exit from the top of cloud, $N_{out,top}$. The cloud bulk reflectivity, Ref_b, whose definition is the fraction of incident radiation reflected, is simply calculated as

$$Ref_b = N_{out,top} / N_{in} \qquad (2.12),$$

where N_{in} is the number of incident photons.

One important thing worthy of mentioning is equation (2.12) does not contradict to the common definition of reflectivity

$$Ref_b = F^{\uparrow}{}_{cld,top} / F^{\downarrow}{}_{cld,top} \qquad (2.13),$$

where $F^{\uparrow}{}_{cld,top}$ is the upward flux density (irradiance) at cloud top, and $F^{\downarrow}{}_{cld,top}$ is the downward flux density at the cloud top.

2.2.3 Statistics

Another question arises naturally after equation (2.12). How many incident photons do we need to input in order to get a satisfying reflectivity? Or how many incident photons N_{in} are necessary to make the standard deviation of reflectivity small enough? To answer this question, we have to move our focus from the random walk of photons inside the cloud to the definition of reflectivity.

In the case of infinite homogeneous cloud, cloud reflectivity at any point, which is constant all over the cloud, has the same value as the cloud bulk reflectivity. Regardless of the complicated random walk trajectories of photons, reflectivity is the probability that an incident photon is reflected. From this point of view, an incident photon being either reflected or transmitted is similar to toss a coin whose chance for head or tail is uneven; say, head is for a photon being reflected. Thus the Gaussian approximation to the binomial distribution is applicable to describe its statistics (Welch and Wielicki, 1984; Lenoble, 1985):

$$\sigma = [Ref_b\,(1 - Ref_b) / N_{in}]^{1/2} \qquad (2.14)$$

, where σ is the standard deviation. The largest value of σ for the same number of incident photons occurs at $R = 0.5$. When $R = 0.5$ and $\sigma = 0.01$, N_{in} is about 2500.

Table (2.1) lists the reflectivity and transmissivity computed by our Monte Carlo code in comparison with those computed by the doubling method. Only 2500 photons were input for each Monte Carlo calculation. Our results show good agreement with the doubling method especially when the optical depth is more than 0.25. Note that we have listed both the value and the percentage of discrepancies. Special caution is necessary for those cases with small reflectivity; the percentage of differences may be drastically large, even though the absolute value for differences are not off much. However, the fact that

	tau \ mu	0.1	0.3	0.5	0.7	0.9
Monte Carlo	0.25	0.4348	0.1972	0.1024	0.0524	0.0372
Doubling		0.4161	0.1580	0.0718	0.0380	0.0225
Difference		0.0187	0.0393	0.0306	0.0144	0.0147
Difference (%)		4.49%	24.85%	42.64%	37.86%	65.33%
Monte Carlo	1.00	0.5872	0.3928	0.2400	0.1528	0.1080
Doubling		0.5815	0.3857	0.2405	0.1502	0.0967
Difference		0.0057	0.0071	-0.0005	0.0026	0.0113
Differece(%)		0.98%	1.84%	-0.20%	1.74%	11.66%
Monte Carlo	4.00	0.7368	0.6176	0.5192	0.4268	0.3568
Doubling		0.7325	0.6173	0.5193	0.4295	0.3482
Difference		0.0043	0.0003	-0.0001	-0.0026	0.0086
Difference(%)		0.58%	0.05%	-0.02%	-0.62%	2.46%
Monte Carlo	16.00	0.8760	0.8188	0.7896	0.7504	0.7000
Doubling		0.8810	0.8300	0.7866	0.7462	0.7072
Difference		-0.0050	-0.0112	0.0030	0.0042	-0.0072
Difference(%)		-0.57%	-1.34%	0.38%	0.57%	-1.02%

Table (2.1) A comparison of reflectivity calculated by the Monte Carlo method and the doubling method. The difference is calculated by reflectivity (Monte Carlo method) minus reflectivity (Doubling method). The difference in percentage form is calculated by dividing the difference of the two methods over the reflectivity calculated by the doubling method. μ_0 is equal to the cosine of the incident zenith angle. In all of these calculations, $\varpi_0 = 1$ and $g = 0.75$.

the larger discrepancies occur at all the small optical depths (when the optical depth is 0.25) or reflectivity is less than 0.1 instead of when the reflectivity is around 0.5 (for example, when the optical depth is 4 and the cosine of the incident zenith angle is 0.5, or when the optical depth is 1 and the cosine if the incident zenith angle is 0.1) suggests some deficiency in the application of the Gaussian statistics to the Monte Carlo method.

2.3 The Monte Carlo Method for Horizontally Inhomogeneous, Non-absorbing Clouds

2.3.1 Computational Procedure

Our use of the term "horizontally inhomogeneous cloud" primarily denotes that $b_{ext,\lambda}$ varies horizontally or / and cloud geometry needs to be considered. The logic of the procedure for horizontally inhomogeneous clouds is pretty much the same as that for the homogeneous cloud deck. The differences are described below.

When $b_{ext,\lambda}$ is not constant, the mean free path is not constant either. For simplicity's sake, consider first a photon traveling from medium A to medium B (Figure 2.3.a), where $b_{ext,\lambda,A}$ is the extinction coefficient for medium A, and $b_{ext,\lambda,B}$ for medium B. Both $b_{ext,\lambda,A}$ and $b_{ext,\lambda,B}$ are constant. Following equation (2.8), a somewhat more complicated expression for the photon free path l can be determined:

$$l = \overline{OF} = \overline{OM} + \overline{MF}$$

$$= \overline{OM}\left(1 - \frac{b_{ext,\lambda,A}}{b_{ext,\lambda,B}}\right) + \frac{1}{b_{ext,\lambda,B}} \ln\left(\frac{1}{\mathcal{R}_i}\right), \qquad (2.15)$$

where R_i is a random number between zero and unity.

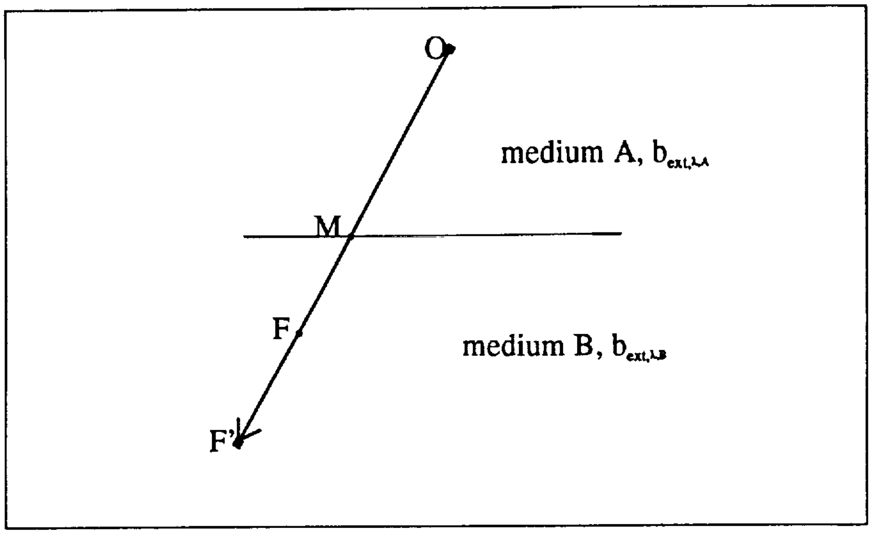

Figure (2.3.a) A schematic diagram of a free path: O is the position of the (i-1) collision; M is the interface point of medium A and medium B in the free path; F' is the position of the i collision. F is the i collision location if the free path is not calculated discretely.

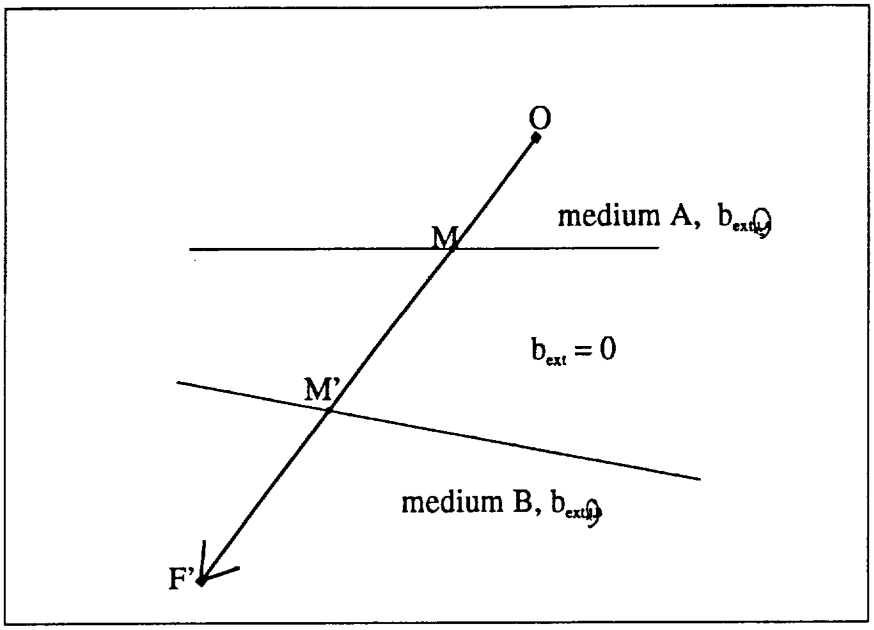

Figure (2.3.b) A schematic diagram of a free path: O is the position of the (i-1) collision; M is the interface point of medium A and the clear region in the free path; M' is the interface point of medium B and the clear region in the free path; F' is the position of the i collision.

If $b_{ext,\lambda}$ is not constant, one of the possible way to handle the free path is by a discrete method. We can divide the medium into boxes in which $b_{ext,\lambda}$ is a slow varying variable. Thus, $b_{ext,\lambda}$ can be seen as a constant in each box. Finally, l can be solved exactly the same way as equation (2.15). Unfortunately, calculating l discretely uses considerable computer time. In this research, we use the extinction coefficient at the (i-1) collision as an average extinction coefficient between the (i-1) collision and the i collision. In another word, we use $\overline{OF}$ as the free path of $\overline{OF}$. The drawback of this simplification is discussed in Chapter 4.

As for the consideration of cloud shapes, it is actually an extreme case of $b_{ext,\lambda}$ variability. We define the cloudy region as $b_{ext,\lambda} \neq 0$, and the clear region as $b_{ext,\lambda} = 0$. Thus, we can draw an imaginary interface between the cloudy and clear regions, which depicts the shape of clouds. Even though in the real world there is no such thing as an absolute interface to separate the clear and cloudy regions but a sharp decline of liquid water content (LWC) at the edge of clouds, we think this way of defining cloud shape serves as a satisfying approximation to study the effects of cloud geometry to the radiation field.

Hence, when photons travel in the clear region, they would never collide with any cloud particles. Take the previous example of a photon traveling from medium A to medium B, and insert a clear region between medium A and medium B (Figure 2.3.b). The free path is just:

$$l = \overline{OF} = \overline{OM} + \overline{MM'} + \overline{MF'}$$

$$= \overline{OM}\ (1 - \frac{b_{ext,A}}{b_{ext,B}}) + \frac{1}{b_{ext,B}} \ln (\frac{1}{R_i}) + \overline{MM'} \qquad . (2.16)$$

Irregularity is the trade mark of cloud shapes; however, the general pattern of cloud shapes is of the main interest in our study. We can divide the cloud shapes present in the literature into three categories: (1) an isolated block (Davies, 1978; McKee and Cox, 1974); (2) organized and pattern-repeated cloud group (for instance, Blerkom, 1971; and Welch and Wielicki, 1984); (3) stochastic cloud patterns (Zuev et al., 1987). The stratocumulus clouds that we simulate in this study are well fitted by the category 2.

In this study, our principles for handling different shapes of clouds are quite similar to Welch and Wielicki's research (1984); however, we add a few procedures as follows:

1. Determine the smallest element of the alignment pattern called the unit cell (Figure 2.4). The highest point of the cloud is set to be Z_{top}.

2. Regardless of the variation of cloud height in this element, divide this element into boxes of equal size (Figure 2.4).

3. Insert N_{in} photons into each box at the center of each box at Z_{top}. Calculate the location that photons would enter into the cloud as the starting point of the photon tracking process.

4. Track photons.

5. If a photon leaves the cloud, check if it would enter the adjacent cloud element or if it has already been reflected or transmitted.

6. Calculate the free path of a photon that crosses the clear region.

7. Apply the concept of periodic boundary conditions so that a photon that enters an adjacent unit cell is wrapped around to re-enter the original cloud unit cell (Figure 2.4).

8. Go back to step 4.

9. After tracking all the photons, count the number of photons exiting from the top of each box (at Z_{top}).

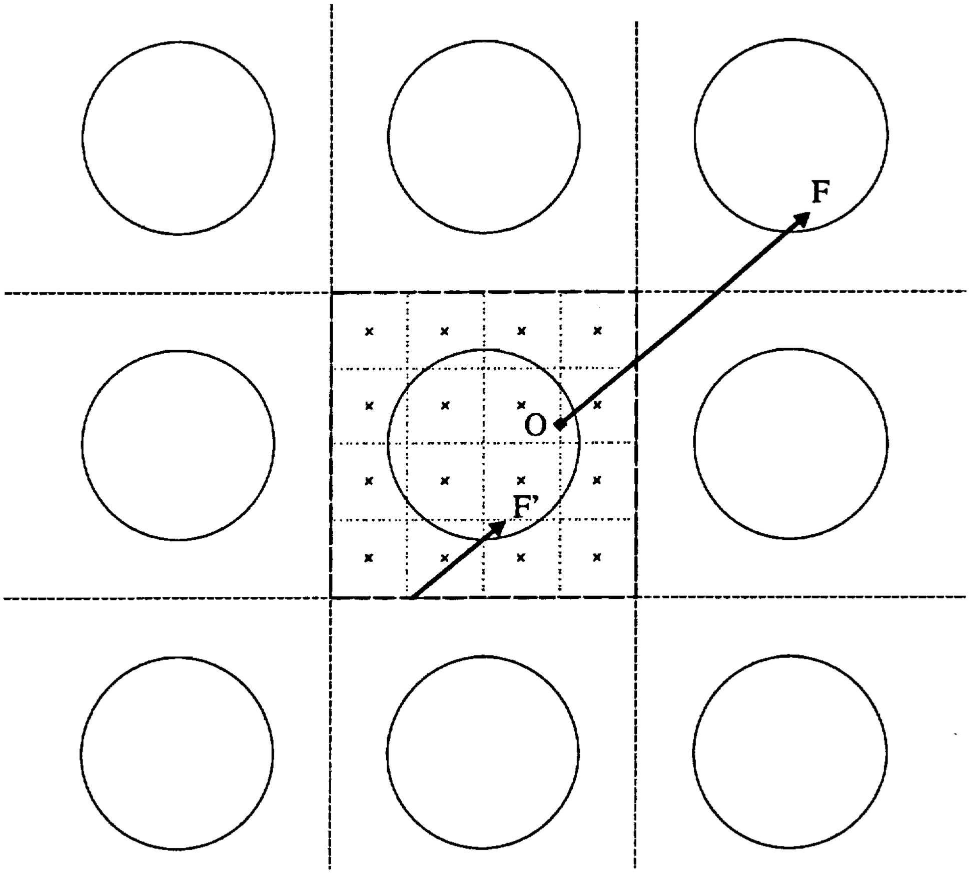

Figure (2.4) A schematic diagram for the unit cell, equal size boxes inside the unit cell, and how photons are wrapped to the unit cell when they go out to adjacent unit cell. In the diagram, the unit cell is uniformly divided into 16 photon collecting boxes. The 'x' marks where incident photons enter the unit cell. A sample of photon wrapping is denoted by the thick line: O is the starting point; F is the real destination; F' is the destination after wrapping.

10. The reflectivity of each box is just $(N_{out,up} / N_{in})_{j \text{ th box}}$. Figure 2.5 is a concise flow chart for the whole procedure.

The bulk reflectivity of this particular cloud pattern is just the mean of the reflectivity of the equal-area boxes, or the total number of photons exiting from the top divided by the total number of photons inserted. Comparisons of our results with Welch and Wielicki's research (1984) are displayed in Figure (2.5) and (2.6).

2.3.2 Statistics

This leads us to the statistics question. What is the size of the photon collecting boxes and the number of incident photons per box needed to capture the 2-dimensional probability density function of reflecting photons, p(x,y; x',y'), which is itself a function of the location where photons are inserted? Here, (x,y) is the location where photons leave the top of the box, and (x',y') is the location where photons are inserted into the cloud element.

To calculate the reflectivity of a homogeneous cloud deck, we just count the photons exiting from the cloud; we don't care where they come out. However, the location where photons exit is important in the case of inhomogeneous clouds.

The analysis of the 2-D distribution of reflecting photons from homogeneous clouds provides a stepping stone for this problem. Figure (2.7.a), (2.7.b), and (2.7.c) respectively show the cumulative spectrums along the x axis, y axis, and the 2-D distribution of photons reflected when 2500 photons are incident on a homogeneous cloud deck at (0,0). Also, the width of the photon collecting boxes is 15 mean free path.

Photons were inserted with a direction pointing toward negative x; hence, the cumulative spectrum along y axis is more symmetric than that along x axis. It is logical to think that if we insert enough photons, we can resolve the 2-D probability density function within satisfactory degree. Moreover, the smaller the collecting box size is, the

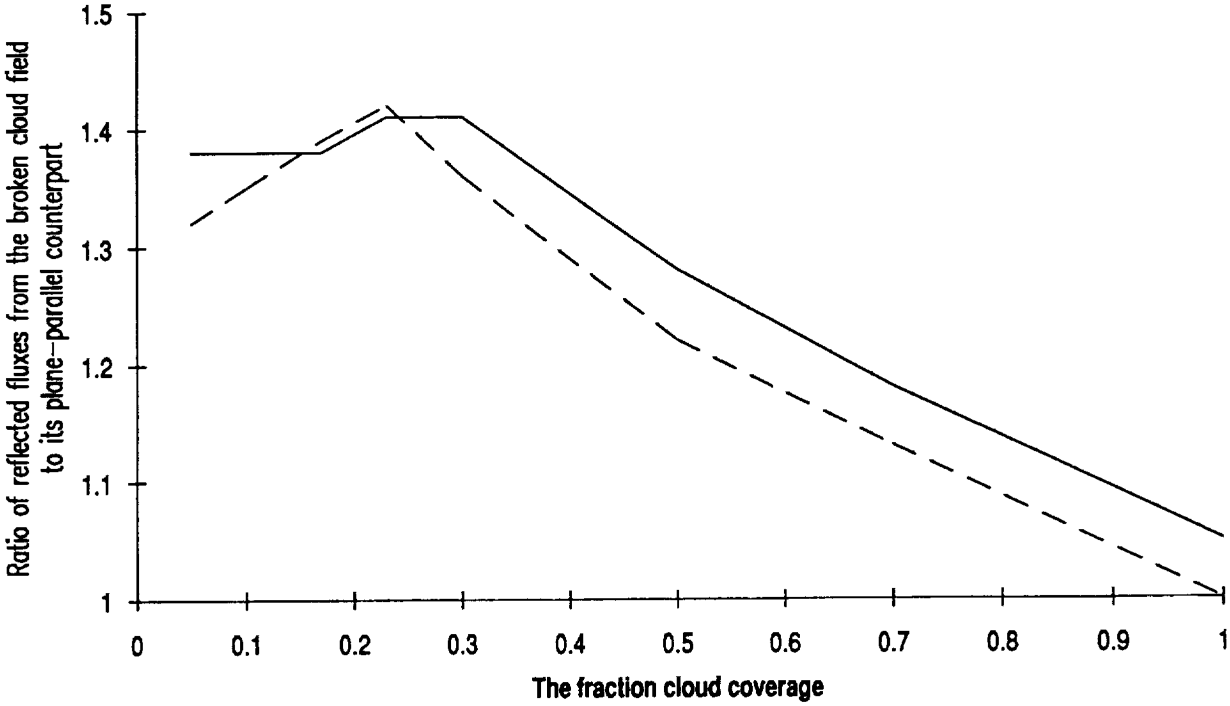

Figure (2.5) Ratio of cubic field radiative fluxes to plane-parallel fluxes as a function of cloud cover: ----- Welch and Wielicki (1984), —— this work. The incident zenith angle = 120°; aspect ratio of the cloud is 1/2, b_{ext} is 49 km^{-1}..

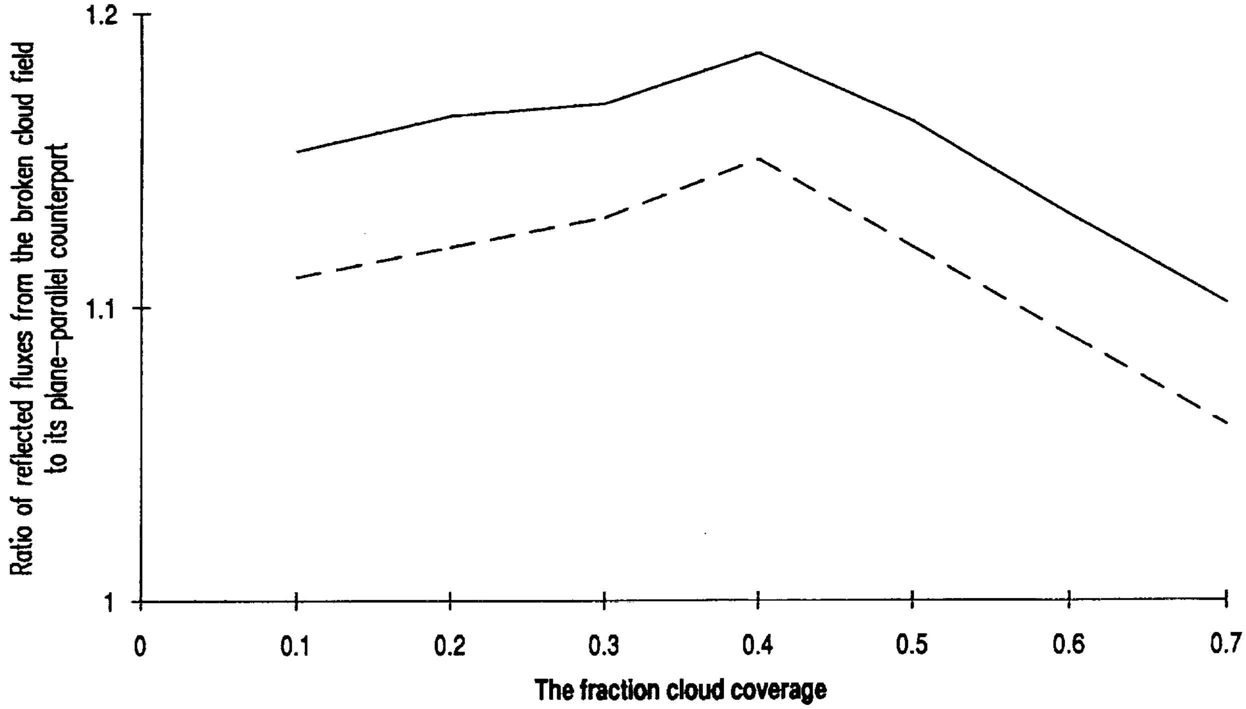

Figure (2.6) Ratio of cloud field fluxes scaled to plane-parallel fluxes as a function of cloud cover for hemispheric clouds: ----- Welch and Wielicki (1984); —— this work. The incident zenith angle = 120°; clouds are hemisphere shaped; b_{ext} is 73 km^{-1}.

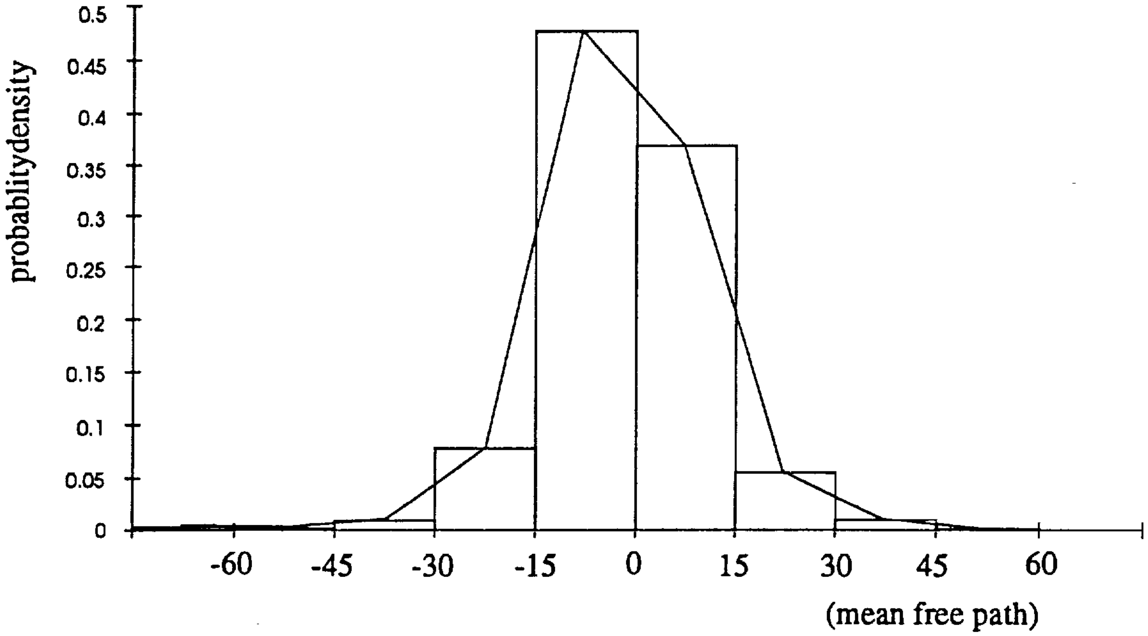

Figure (2.7.a) The cumulative probability density function in the x direction for an infinite, homogeneous, non-absorbing cloud deck. The incident azimuth angle is 15°, the cloud optical depth is 16, g is 0.86.

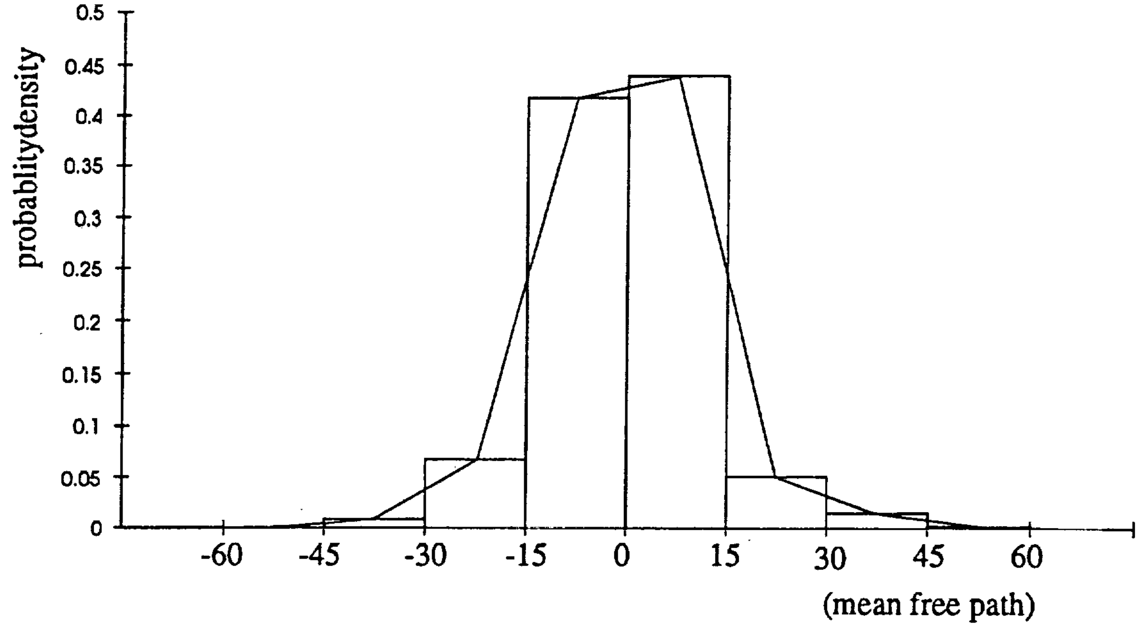

Figure (2.7.b) The cumulative probability density function in the y direction for an infinite, homogeneous, non-absorbing cloud deck. The incident azimuth angle is 15°, the cloud optical depth is 16, g is 0.86.

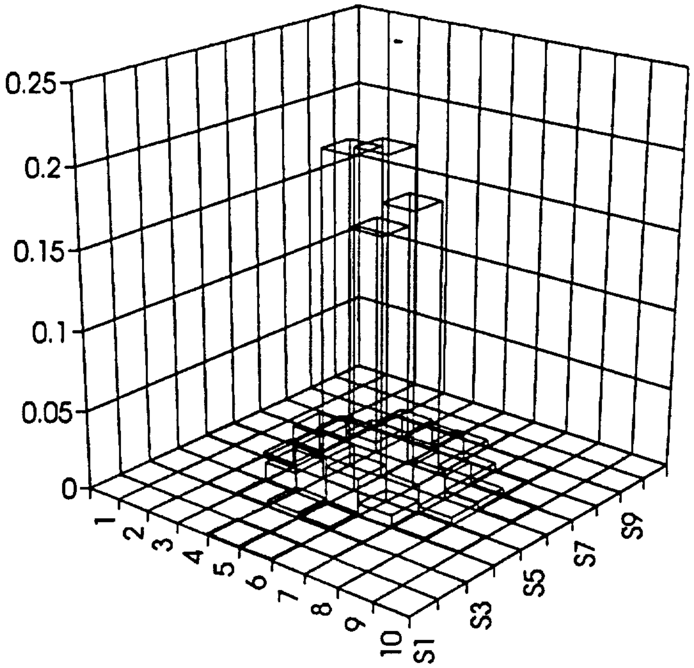

Figure (2.7.c) The 2-D probability density function for an infinite, homogeneous, non-absorbing cloud deck. The incident azimuth angle is 15°, the cloud optical depth is 16, g is 0.86.

more incident photons are needed in order to get the detailed structure of the 2-D probability density distribution.

For inhomogeneous clouds, every point at which photons are inserted into the cloud has its corresponding 2-D probability density function of reflecting photons, but the function is more skewed or asymmetric than that of the homogeneous cloud deck because of cloud geometry or varying $b_{ext,\lambda}$. By overlapping the 2-D probability density functions, that is to say $Ref_p=\int_{-\infty}^{\infty}\int_{-\infty}^{\infty} p(x,y;x',y')dxdy$, we can obtain the reflectivity of each point. In addition, we want the size of the boxes large enough to capture the structure of the 2-D probability function and small enough to capture the geometry of the cloud.

Now we can go back to explain the reason why we don't care where photons come out for the homogeneous cloud deck. Because the 2-D probability distribution is the same for every point in the infinite, homogeneous cloud, overlapping the probability distribution is equal to just counting the reflecting photons. From the above discussion, the Gaussian approximation to the binomial distribution is not applicable to describe the statistics of Ref_b because Ref_p is not a constant. Nor is it suitable for Ref_p, because $Ref_p=\int_{-\infty}^{\infty}\int_{-\infty}^{\infty} p(x,y;x',y')dxdy$.

Chapter 3

FIRE DATA

The radiation and cloud microphysics data collected by the NCAR Electra flight 2, which was carried out on June 30, 1987 during the FIRE marine stratocumulus observations, are of prime interest in this study. A GOES satellite image for flight 2 is shown in Figure (3.1), in which the flight path has been dotted. The cloud field can be categorized as a solid stratocumulus deck with occasional breaks. A lidar flight leg (referred to as leg 5 in the later text) with its corresponding turbulent flight leg (referred as leg 3 in the later text) are chosen for our simulation.

Because of the differences in time and space of these two flight legs (Figure 3.2), we can not overlap the two data sets and obtain the correlation of the microphysics data and radiation data. However, some interesting information can be extracted from these data. Section 3.1 and 3.2 will describe the general cloud condition, and instruments used in leg 3 and leg 5.

3.1. Leg 3

Leg 3, in which the aircraft flew at a mean altitude of 790m above sea level, was carried out from GMT 20:10 (hour:min) to 20:20, which happens to be coincident with the time the satellite image (Figure 3.1) was taken. As it is shown from Figure 3.1 and from the summary of the cloud conditions in (Kloesel et al., 1988), the top of each individual cloud unit was solid, yet the cloud field as a whole was broken.

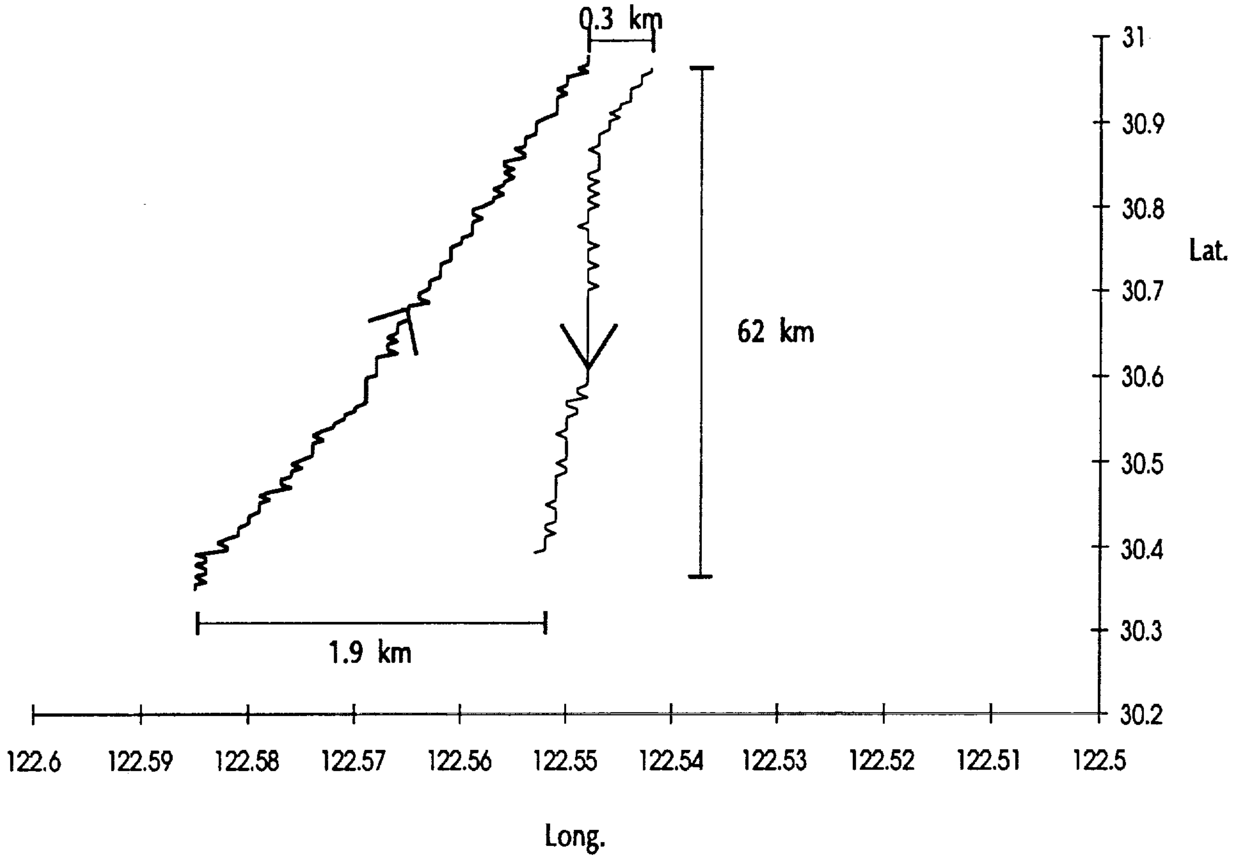

Figure (3.2) The flight paths of leg 3 and leg 5. Arrows denote flight direction.

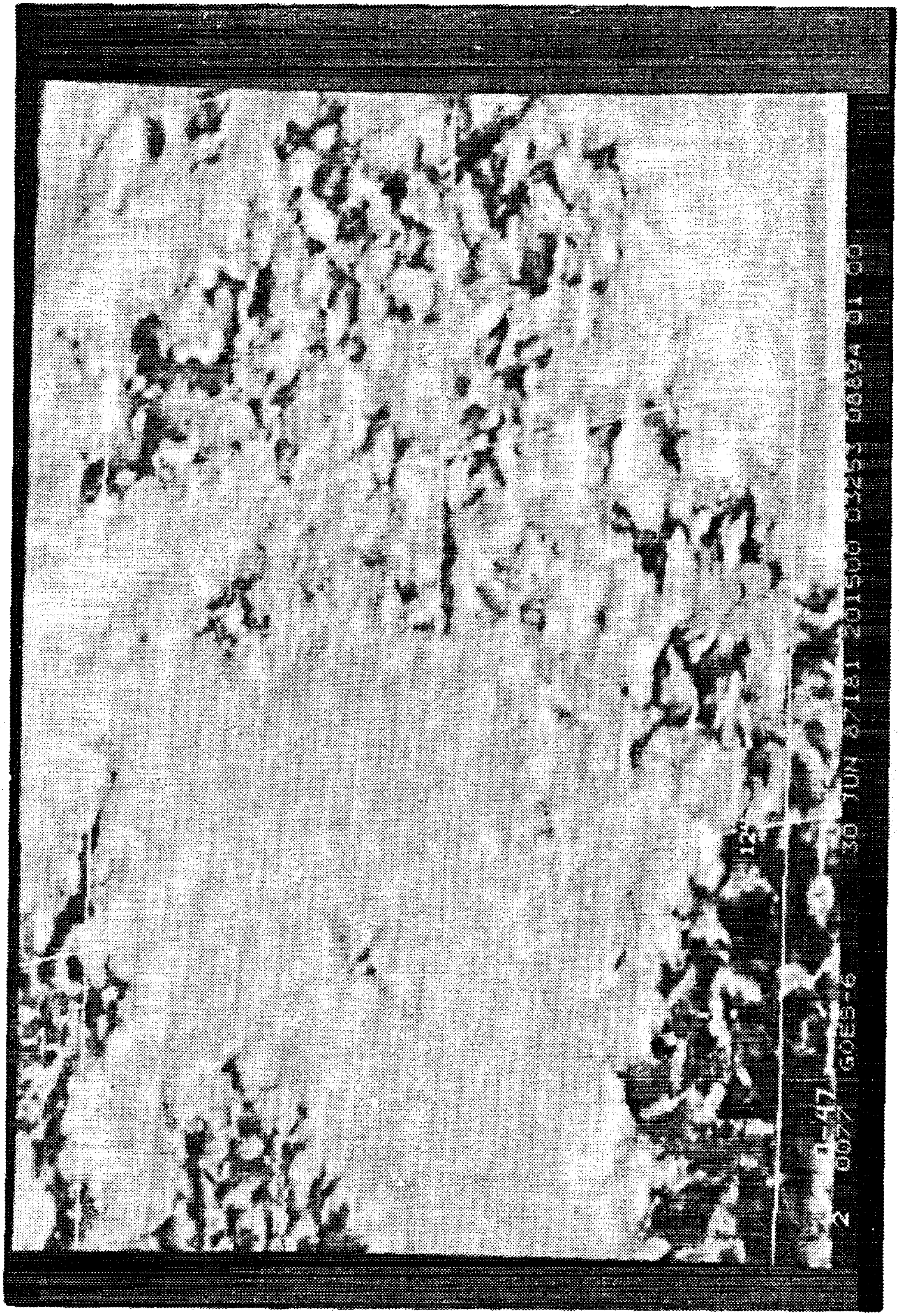

Figure (3.1) The satellite image from GOES.

The cloud microphysics data - the mean diameter ($\bar{d}$), standard deviation (σ), number density (N_d) and the liquid water content (LWC) - measured by the forward scattering spectrometer probe (FSSP) and by the 260X one-dimensional optical array probe are exploited. The FSSP, which has 15 channels, primarily sizes and counts water droplets from 0.5 μm to 45 μm in diameter, while the 260 sizes particles from 10 μm to 620 μm in 10 μm increment.

The definition of $\bar{d}$ and σ follow basic statistics. $\bar{d}$ is simply the arithmetic average of all cloud droplet diameters:

$$\bar{d} = \sum_{i=1}^{m} f_i d_i \qquad (3.1)$$

And σ is calculated as:

$$\sigma = \sqrt{\left(\sum_{i=1}^{m} f_i d_i^2\right) - \bar{d}^2} \qquad (3.2)$$

And LWC is computed by:

$$LWC = \rho_w \frac{\pi}{6} \sum_{i=1}^{m} f_i d_i^3 \qquad (3.3)$$

, where f_i = number density of particles in channel i, d_i = diameter which channel i represents, m = number of channels, and ρ_w = the density of water. And $N_d = \sum_{i=1}^{m} f_i$.

It should be noted that the LWC is not equal to $\rho_w \frac{\pi}{6} \bar{d}^3$. Also, these definitions of $\bar{d}$ and σ are different from the definitions of the geometric mean diameter and the geometric standard deviation of the log-normal distribution of cloud droplets, which is commonly used in calculating the extinction cross section, the asymmetry factor and the single scattering albedo in a standard Mie scattering code. See Section (4.1.1) for detailed illustrations.

Figure (3.3.a) and (3.4) show $\bar{d}$, N_d and LWC measured by the FSSP and by the 260X along leg 3. However, the x axis is intentionally reversed, because the flight directions of leg 3 and leg 5 were opposite (Figure 3.2).

The N_d and LWC in the Figure 3.3.a have the same tendency to increase from cloud edge to cloud center and decrease from cloud center to the opposite cloud edge, especially between 47 km and 39 km, and between 32 km and 27 km. Yet, $\bar{d}$ stays fairly constant inside of these two cloud blocks despite the existence of small fluctuations in its value. The other cloud blocks did not show apparent correlation among $\bar{d}$, N_d and LWC. The $\bar{d}$ and σ are plotted in Figure (3.3.b). The σ was magnified 10 times in order to show its correlation with $\bar{d}$. Inside the two larger clouds (Figure 3.3.b), σ does not change much.

However, $\bar{d}$, N_d and LWC measured by the 260X (Figure 3.4), which is designed to measure the larger cloud droplets, did not demonstrate particular correlation in any of the cloud blocks.

3.2 Leg 5

Leg 5, in which the aircraft flew with a mean altitude of 1400m above the sea surface, or about 530m above the average cloud top height, was conducted from GMT 21:09 to 21:20, approximately one hour after leg 3. The stratocumulus clouds of leg 5 became more solid than the previous flight leg (Kloesel et. al., 1988).

Figure 3.5 shows the equivalent brightness temperature, shortwave broad-band albedo and the cloud top height collected during this flight leg. The equivalent brightness temperature was transformed from the upwelling radiance measured by a 2°-field-of-view nadir radiometer within the atmospheric window region (10 - 12 μm).

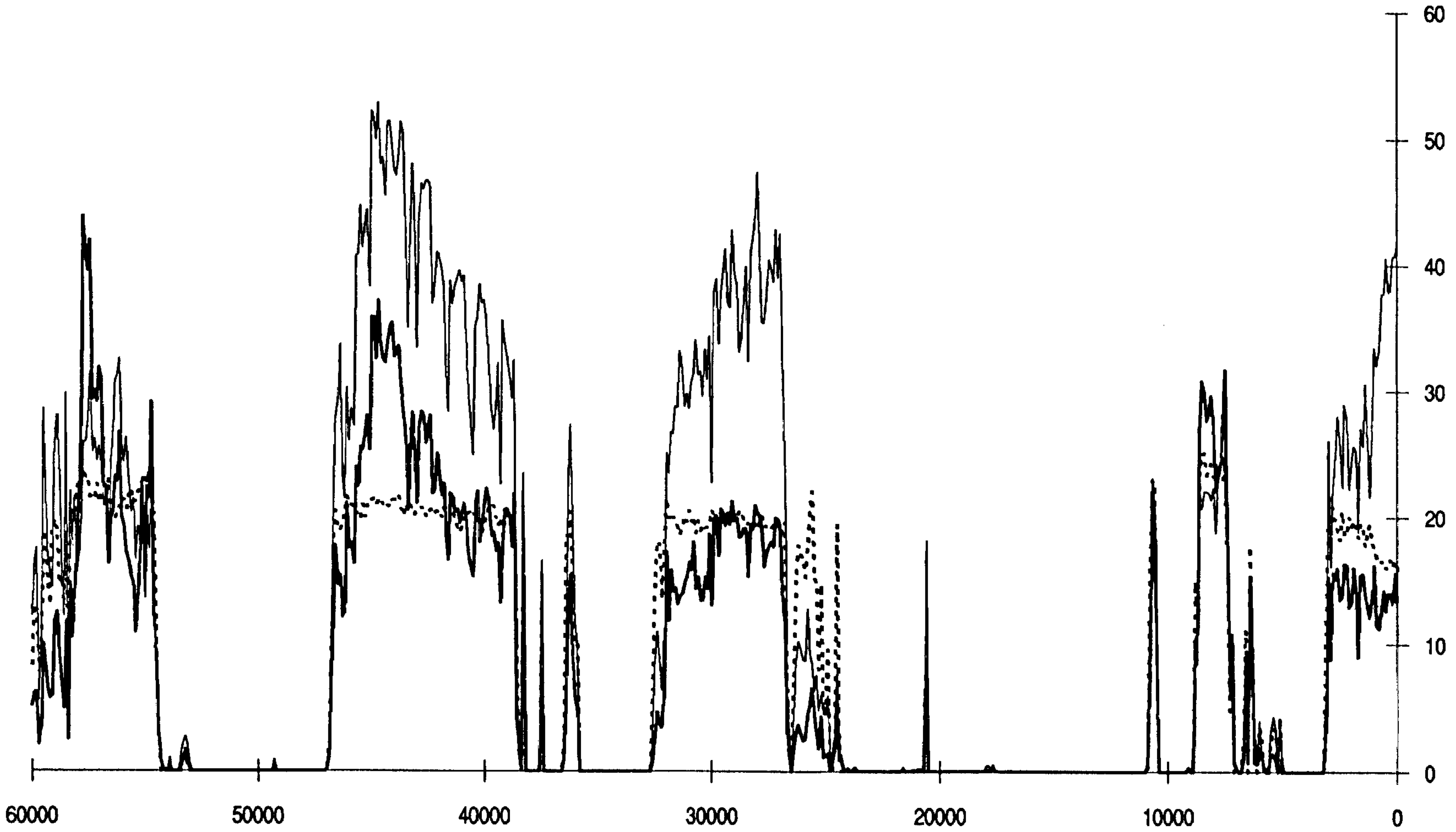

Figure (3.3.a) The number density (in unit of #/cm^3; denoted by the thin solid line), the mean diameter (in unit of μm; denoted by the heavy solid line) and the LWC (in unit of 10^{-2} g/m^3 ; denoted by the heavy dashed line) measured by the FSSP along the NCAR Electra flight 2 leg 3 during FIRE.

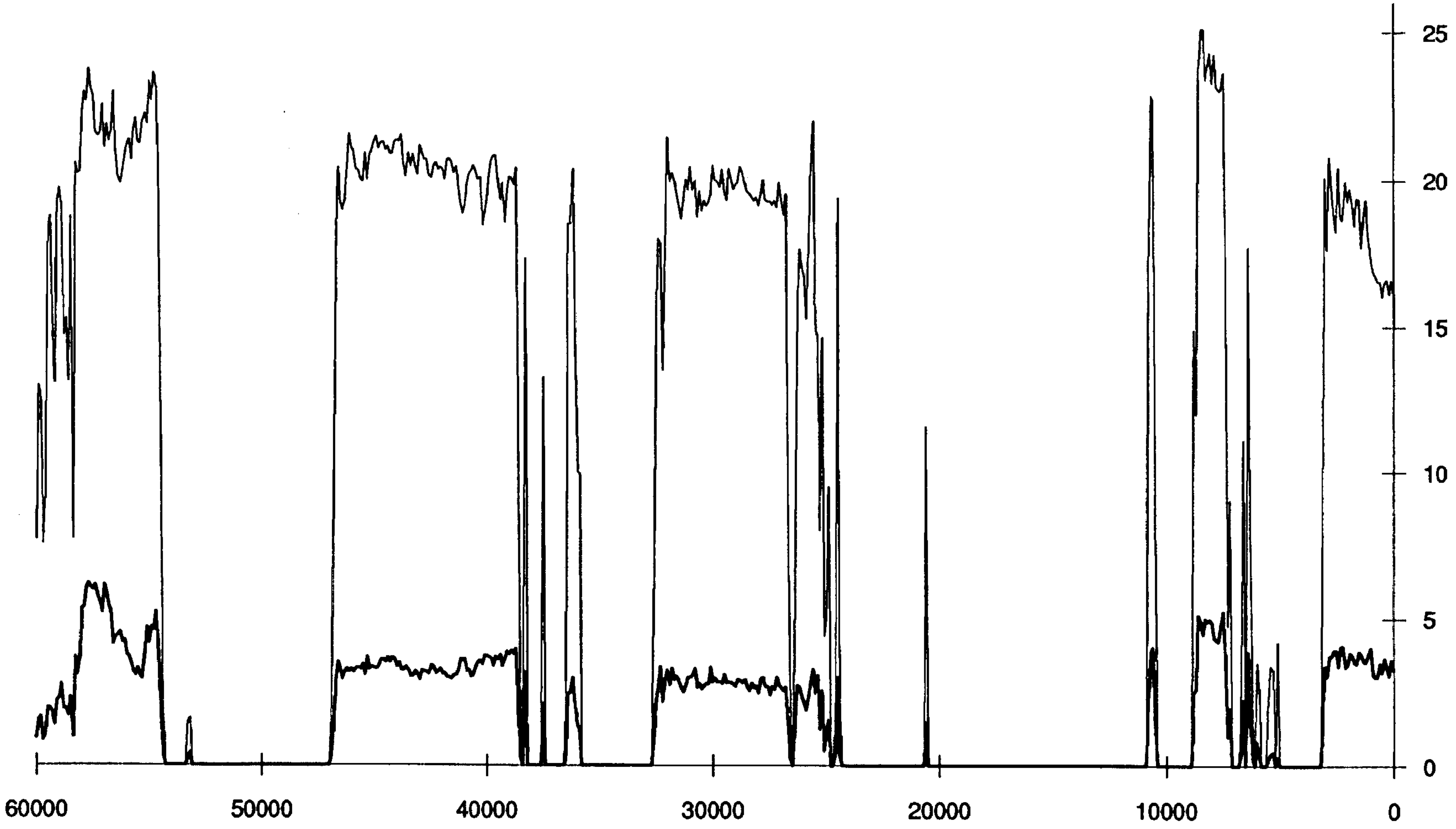

Figure (3.3.b) The mean diameter in unit of μm (denoted by the thin line) and the standard deviation in unit of 10^{-1} μm (denoted by the heavy line) measured by the FSSP along the NCAR Electra flight 2 leg 3 during FIRE.

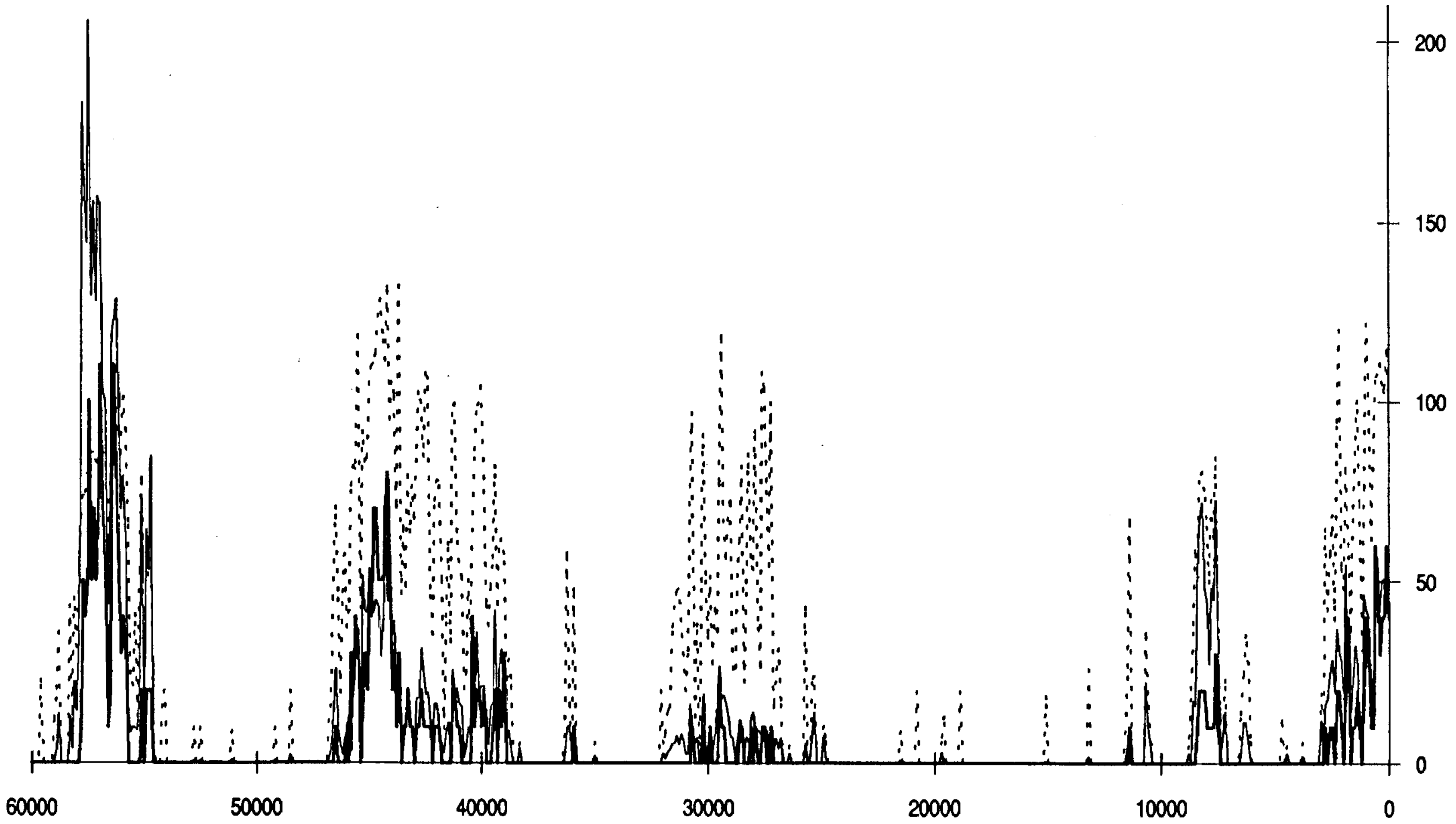

Figure (3.4) The number density (in unit of #/liter; denoted by the thin solid line), the mean diameter (in unit of μm; denoted by the thin dashed line) and the LWC (in unit of 10^{-3}g/m^3; denoted by the heavy solid line) measured by the 260X along the NCAR Electra flight 2 leg 3 during FIRE.

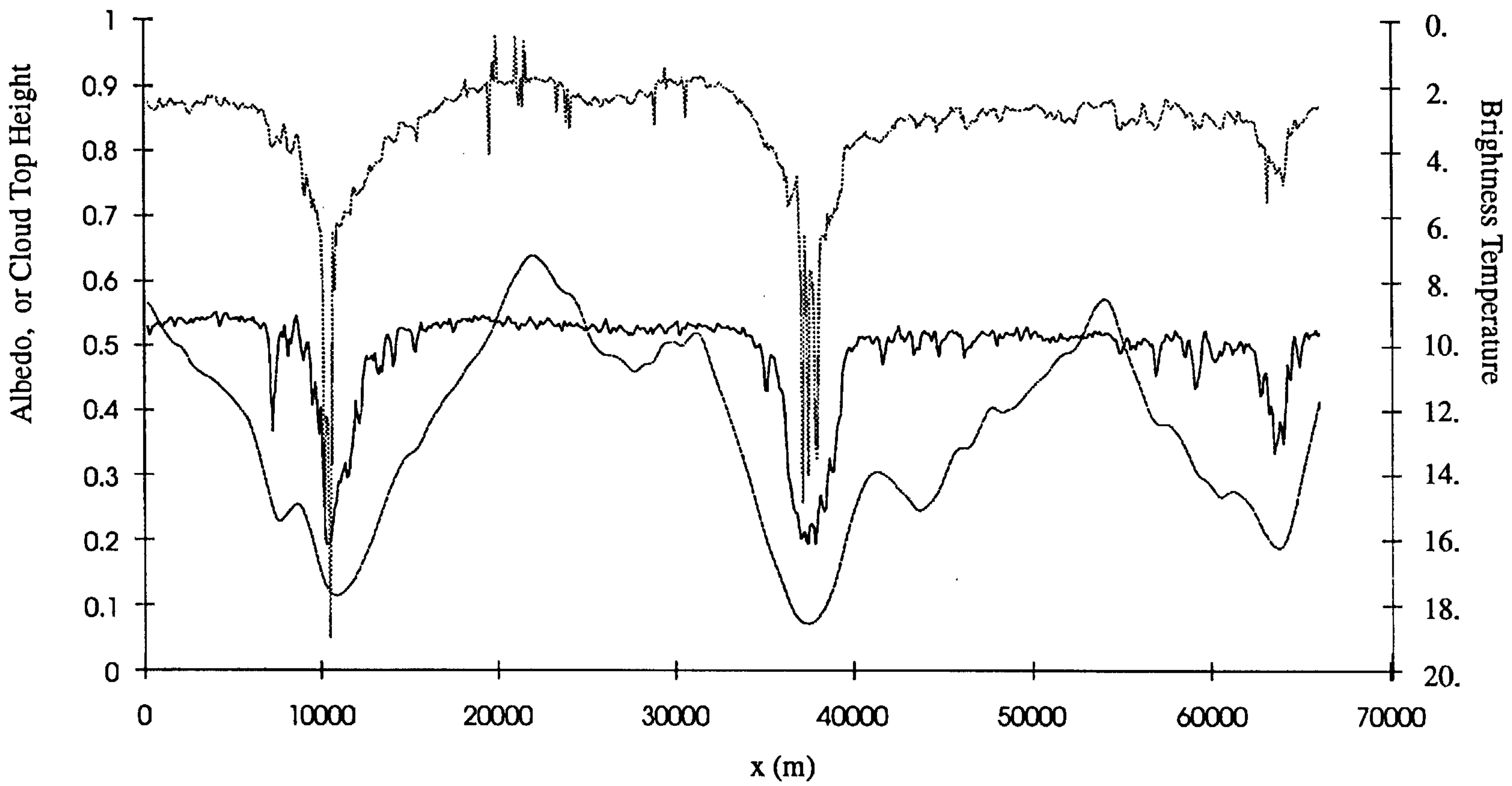

Figure (3.5) The cloud top height, brightness temperature and albedo measured along the path in NCAR Electra flight 2 leg 5 during FIRE: the thin dotted line denotes cloud top height, the solid line denotes brightness temperature, and the thin dotted line denotes albedo.

Shortwave broad-band albedo was calculated by dividing the upward shortwave flux measured by a downward-looking broad-band pyranometer by the downward shortwave flux measured by the similar instrument looking up. It has been verified that the downward flux was rather uniform along the flight path; therefore, there were no clouds necessary to be considered above the stratocumulus cloud deck. A downward looking lidar measured the cloud top height.

As is shown in Figure 3.5, generally, the equivalent brightness temperature shows good positive correlation with the cloud top height. However, at the edge of the clouds, (holes in the cloud field are around 10-11 km and 37-38.5 km in the plot), the slope of the cloud top height is sharper than that of the equivalent brightness temperature. The explanation for this phenomenon is that lidar is a fairly sensitive detector of the existence of cloud droplets. The cloud top height is essentially the height at which the lidar detects a return signal from some volume containing cloud droplets. It is believed that there are still some cloud droplets scattering randomly in the breaks of clouds. Thus, using the cloud top height to infer the shape of cloud could underestimate the width of holes at the cloud top.

The detected brightness temperature, however, relies much more on the cloud optical depth beneath the aircraft. For two clouds with the same LWC but with different number density, the cloud optical depth of the cloud with greater number density is larger. Yet, two clouds with the same number density but with different LWC, the one that contains more liquid water has larger optical depth. At the edge of clouds, the mixing of the moist air of clouds with the dry entrained air could result in a decrease of number density but an increase of the mean diameter. Both of these two changes will cause a decrease of the cloud optical depth at the edge of clouds.

The most interesting feature of Figure 3.5 is that the albedo changes drastically from 0.1 to 0.65 while cloud top height and equivalent brightness temperature are fairly smooth except at the edge of clouds. The albedo maxima at 20 km and 30 km are coincident with the two small increments in cloud top height in the second cloud, whereas no obvious cloud top maximum is observed corresponding to the albedo maximum of the third cloud. It can also be recognized easily that the albedo declines almost linearly from the peak to the trough, or from the center of clouds to the edge of the clouds.

The decrease of albedo at the cloud edge could result from the decrease of the optical depth at the cloud edge. Moreover, some photons which were originally inserted on clouds will leak out at vertical sides at the cloud edges causing additional decrease of albedo. The following chapter will discuss these two assumptions based on our simulation results.

Chapter 4.

Simulation Results

Our motivation for the simulation originated from the plots of solar reflectivity and cloud top height along the flight path of FIRE Electra flight 2 Leg 5 (Figure 3.5). As it is shown on the figure, the cloud top height except at the edge of the cloud is rather uniform while the solar reflectivity shows a wave like pattern, which has its trough at the hole and its ridge at the cloud center.

Two factors could contribute to this phenomenon: the geometry and the alignment pattern of clouds, and the variation of cloud optical properties inside the cloud. The goal of these simulations is to identify which of the two factors is more important in this case.

4.1 Strategy

Basically, two types of cloud field are used in our simulations of the visible radiation field. The cloud geometry and alignment pattern are considered in all of our Monte Carlo simulation experiments, but each experiment is with different degree of geometry effect. However, b_{ext} remains constant in the first type of experiments, but it varies in space in a specified pattern in the second type. By comparing the result of each experiment with the observational data, we can obtain insight to the above cloud shape versus cloud optical properties problem.

Meanwhile, the IR observational data can serve as an additional check to our simulations. We can calculate the IR radiation field corresponding to each simulation experiment and compare it with the observational data. Beside this, we can also check our assumptions of optical properties of the clouds with the cloud microphysical properties observed.

In order to fulfill the comparisons mentioned above, a standard Mie scattering code, the IR hemispheric mean code, and a flux extrapolation scheme are introduced into this study. The following sub-sections briefly discuss these schemes.

4.1.1 Mie scattering code

The volume extinction cross section σ_{ext} (unit = $[L^2]$), the asymmetry factor g, and the single scattering albedo ϖ_0 of a specified log-normal distribution with geometric mean radius r_g and geometric standard deviation σ_g are calculated by the Mie scattering code. The log-normal distribution of cloud droplets is assumed as follows:

$$N(\ln r) = \frac{1}{\sqrt{2\pi}\ln\sigma_g}\exp[\frac{-1}{2}(\frac{\ln r - \ln\overline{r_g}}{\ln\sigma_g})^2] \qquad (4.1).$$

The relation between $\bar{r}$, the mean radius of cloud droplets ($\bar{d}/2$, $\bar{d}$ is defined in Section 3.1) and r_g is $\bar{r} = r_g \exp[0.5(\ln\sigma_g)^2]$, when the log-normal distribution of clouds is applicable.

The theory of Mie scattering is not reviewed here. This sub-section only focuses on how we choose reasonable values for $r_g$and σ_g to obtain satisfying values of σ_{ext}, g, and ϖ_0.

Figure (4.1) series show plots of contours of σ_{ext} and g at 0.6 μm for different r_g and σ_g. ϖ_0 is not shown because it ranges from 0.999988 to 0.999999. The range of r_g and σ_g in the plots covers a plausible range of r_g and σ_g in stratiform, non-precipitating water clouds. We can conclude that, for this type of cloud, the spectrum of cloud droplet

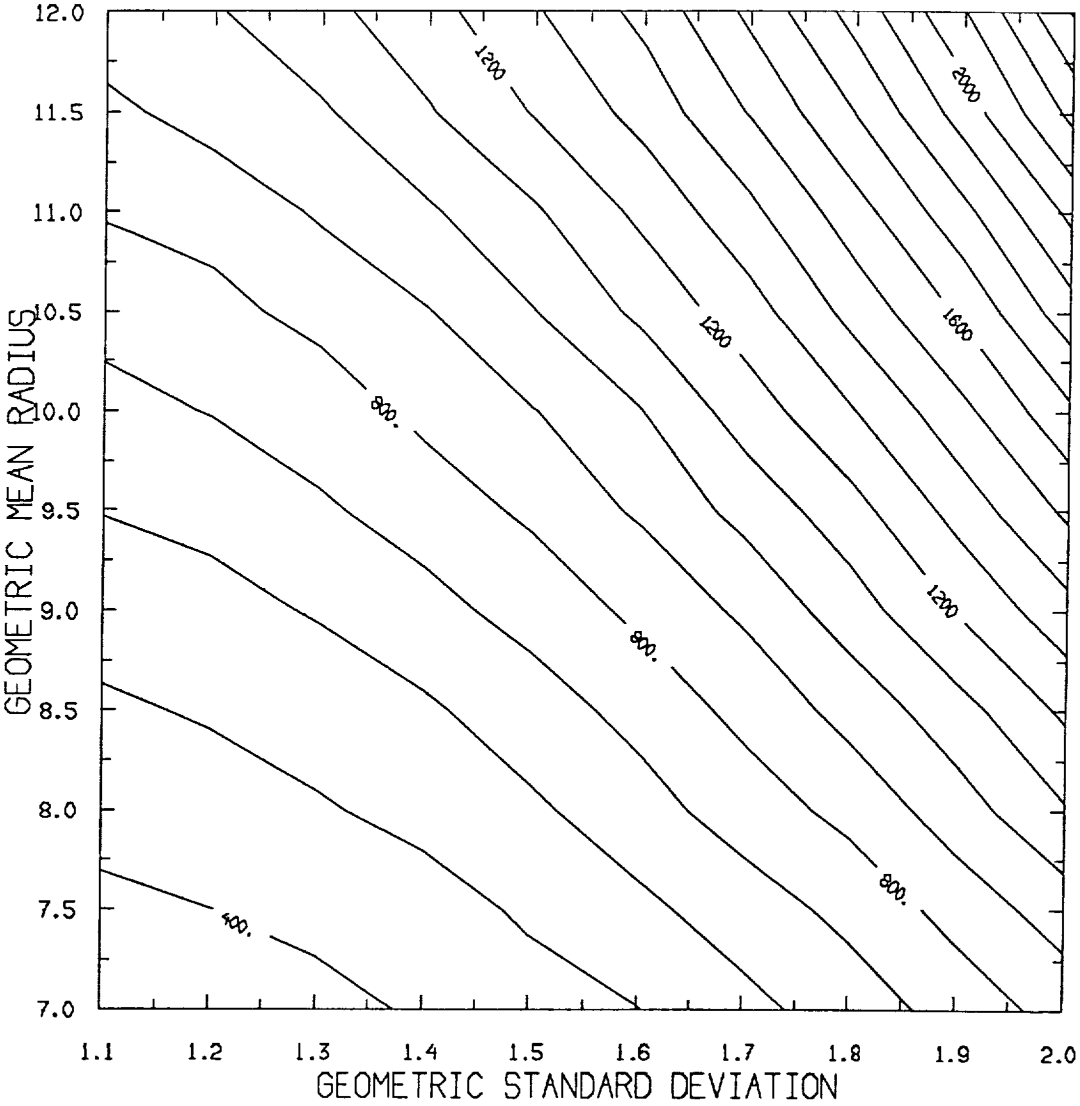

Figure (4.1.a) The contours of volume extinction cross section at 0.6 μm as a function of the geometric mean radius and the geometric standard deviation. Contour minimum: 300 μm^2; maximum: 2400 μm^2; increment between two contours: 100 μm^2.

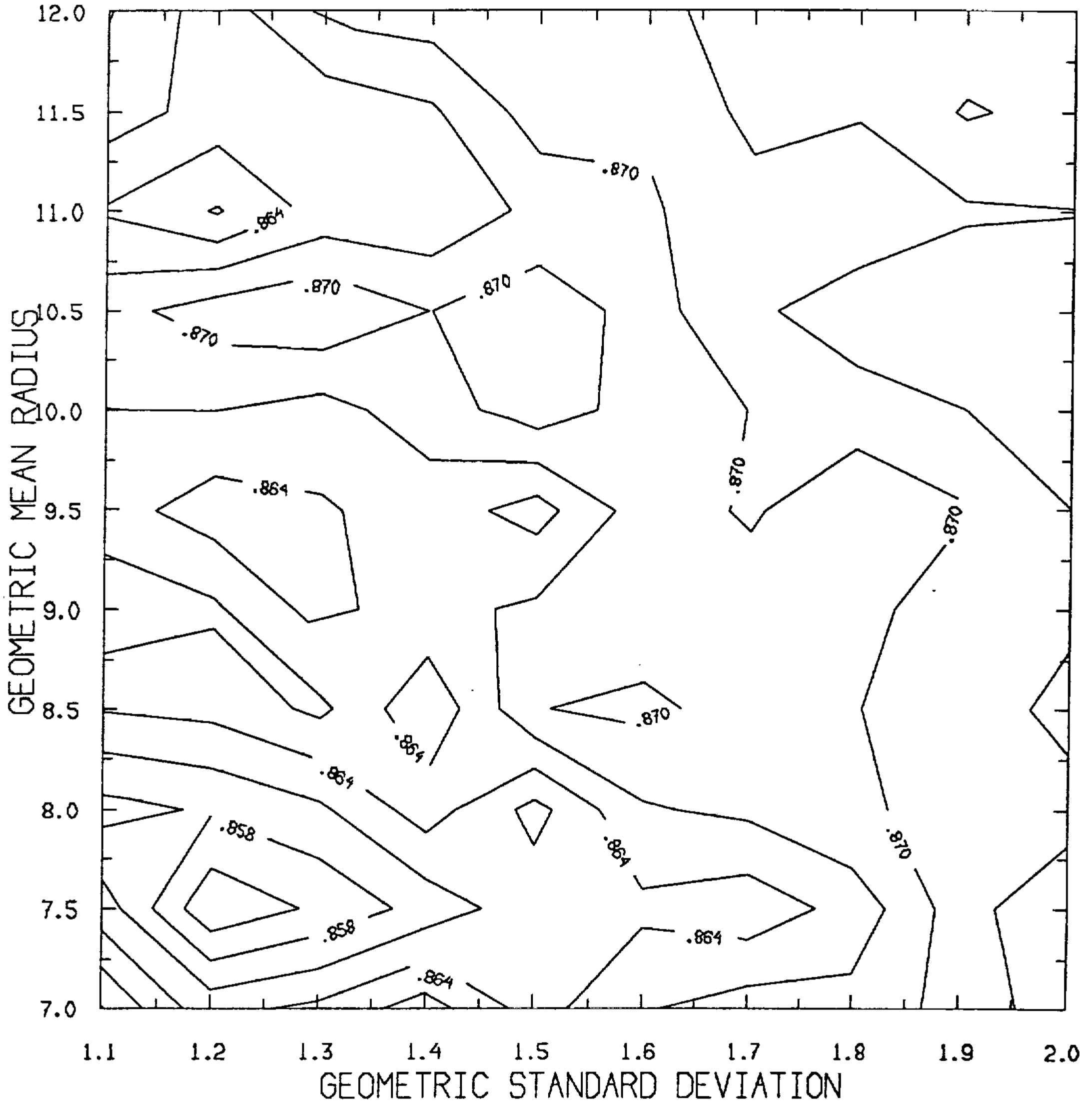

Figure (4.1.b) The contours of asymmetric factor at 0.6 μm as a function of the geometric mean radius and the geometric standard deviation. Contour minimum: 0.852; maximum: 0.976; increment between two contours: 0.003.

distribution does not affect the value of g and ϖ_0 much. The values $\varpi_0 = 1$ and $g = 0.86$ are fairly reasonable.

However, the contours of σ_{ext}, g, and ϖ_0 at 10 µm are rather complicated. (Figure 4.2) We shall examine how we choose representative values of σ_{ext}, g, and ϖ_0 for our IR check in section 4.5.

All the values of refractive index for water in this study are from Hale and Querry (1973).

4.1.2 The Hemispheric Mean 2-Stream Technique

The Monte Carlo method is more complicated for IR radiation because the emission of photons also has to be considered. Therefore, the hemispheric mean 2-stream technique is selected to give us a first degree of approximation of the IR radiation field of a horizontally inhomogeneous cloud. The details of the hemispheric mean technique is described in Toon et al., 1989. A few approximations are made when the technique is applied to the calculation of IR field.

First, we assumed that the temperature in the cloud deck is constant. This is actually a reasonable approximation. The value of a saturated adiabatic lapse rate at these temperatures is around 6°C in the lower troposphere; thus, for a cloud deck whose depth is only 200 to 300 meters, the change of temperature from cloud bottom to cloud top is only around 1.5 °C.

Second, the ocean is assumed to be a blackbody. In another words, the absorptivity and emissivity of the surface are equal to 1 in our IR calculation.

Then, we can write the equations as follows:

$$F = k_1 e^{\varepsilon\tau} + \Gamma k_2 e^{-\varepsilon\tau} + C^+ \qquad (4.2),$$

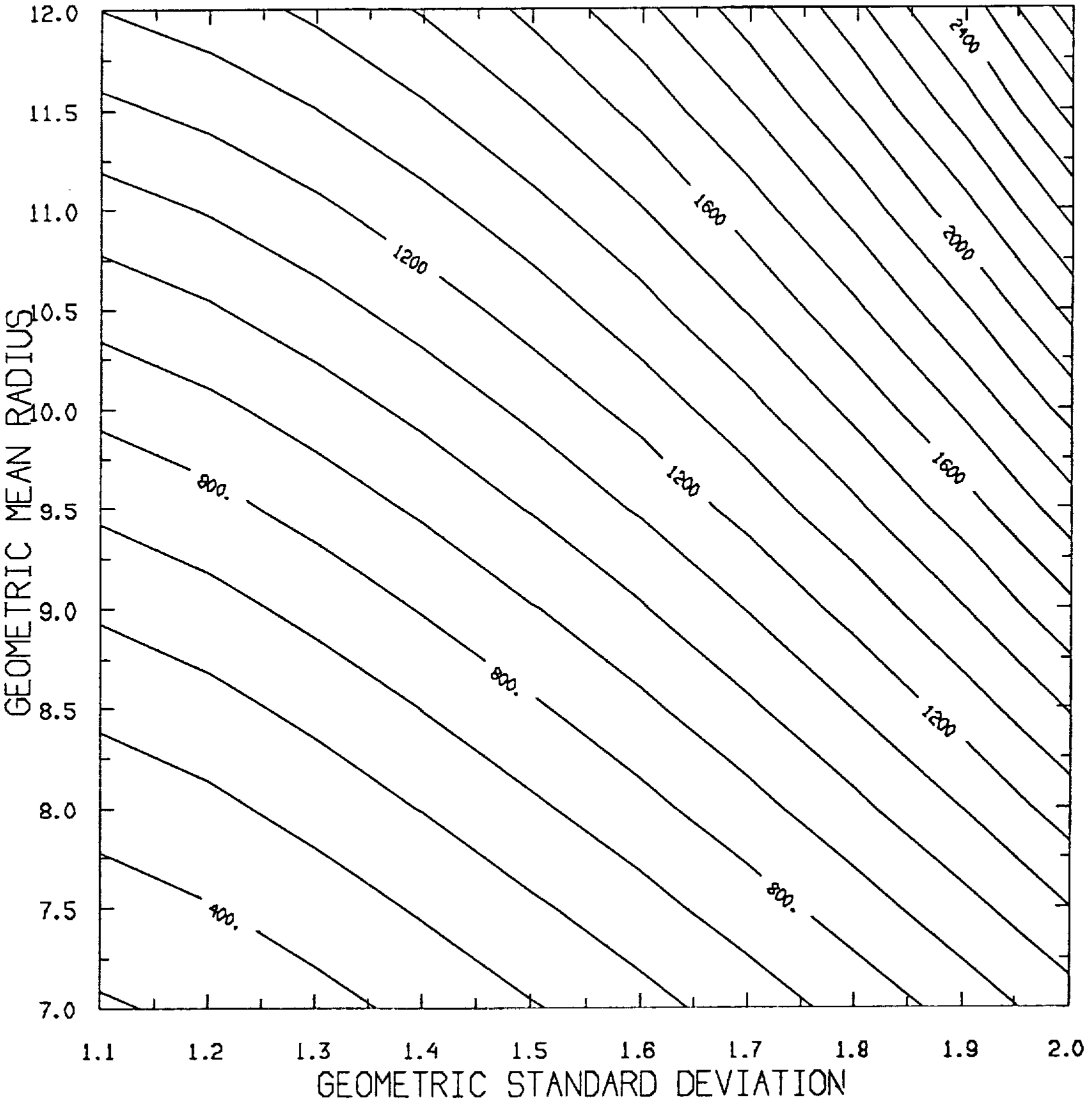

Figure (4.2.a) The contours of volume extinction cross section (μm^2) at 10 μm as a function of the geometric mean radius and the geometric standard deviation. Contour minimum: 200 μm^2; maximum: 2700 μm^2; increment between two contours: 100 μm^2.

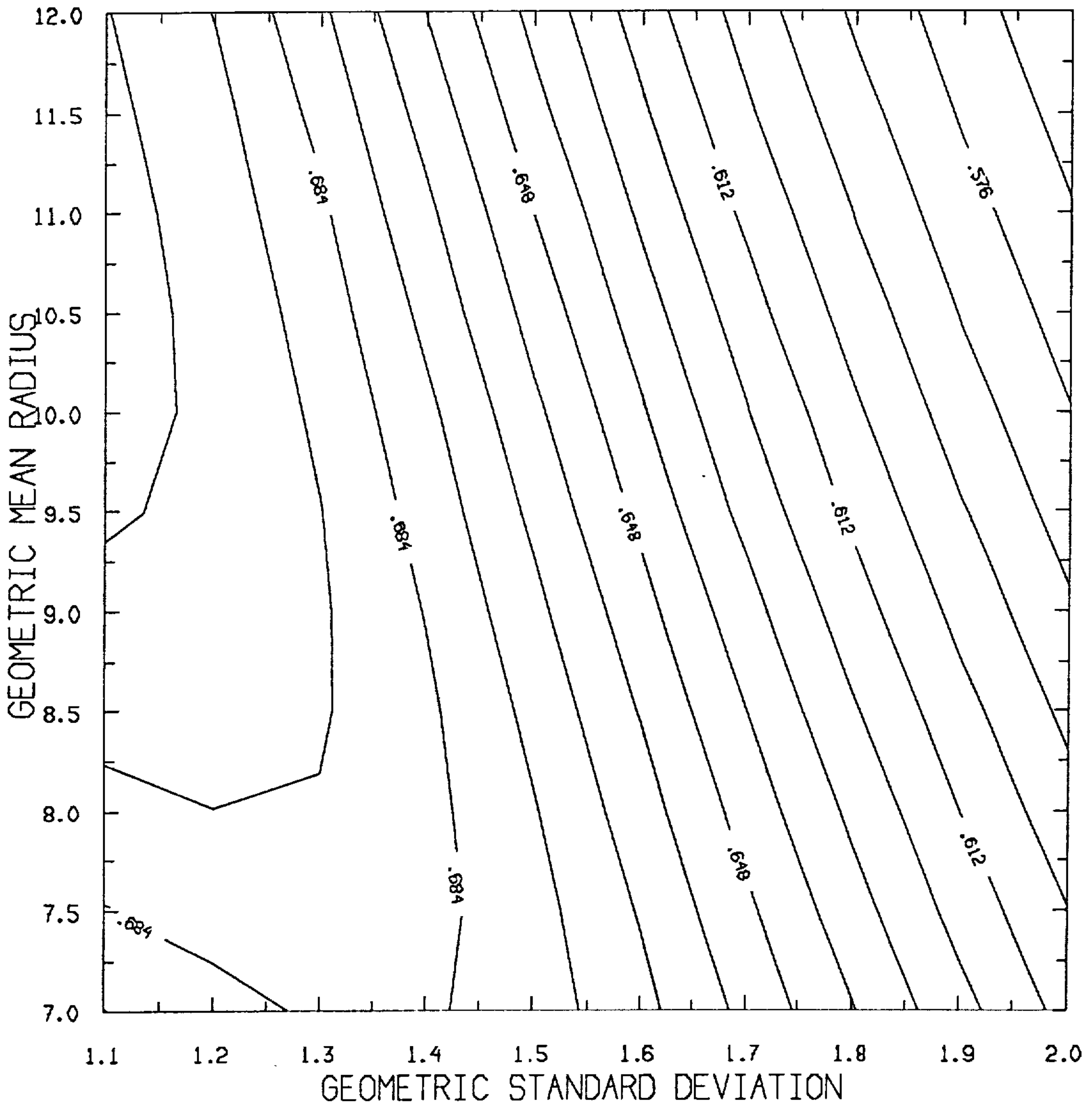

Figure (4.2.b) The contours of single scattering albedo at 10 μm as a function of the geometric mean radius and the geometric standard deviation. Contour minimum: 0.558; maximum: 0.702; increment between two contours: 0.009.

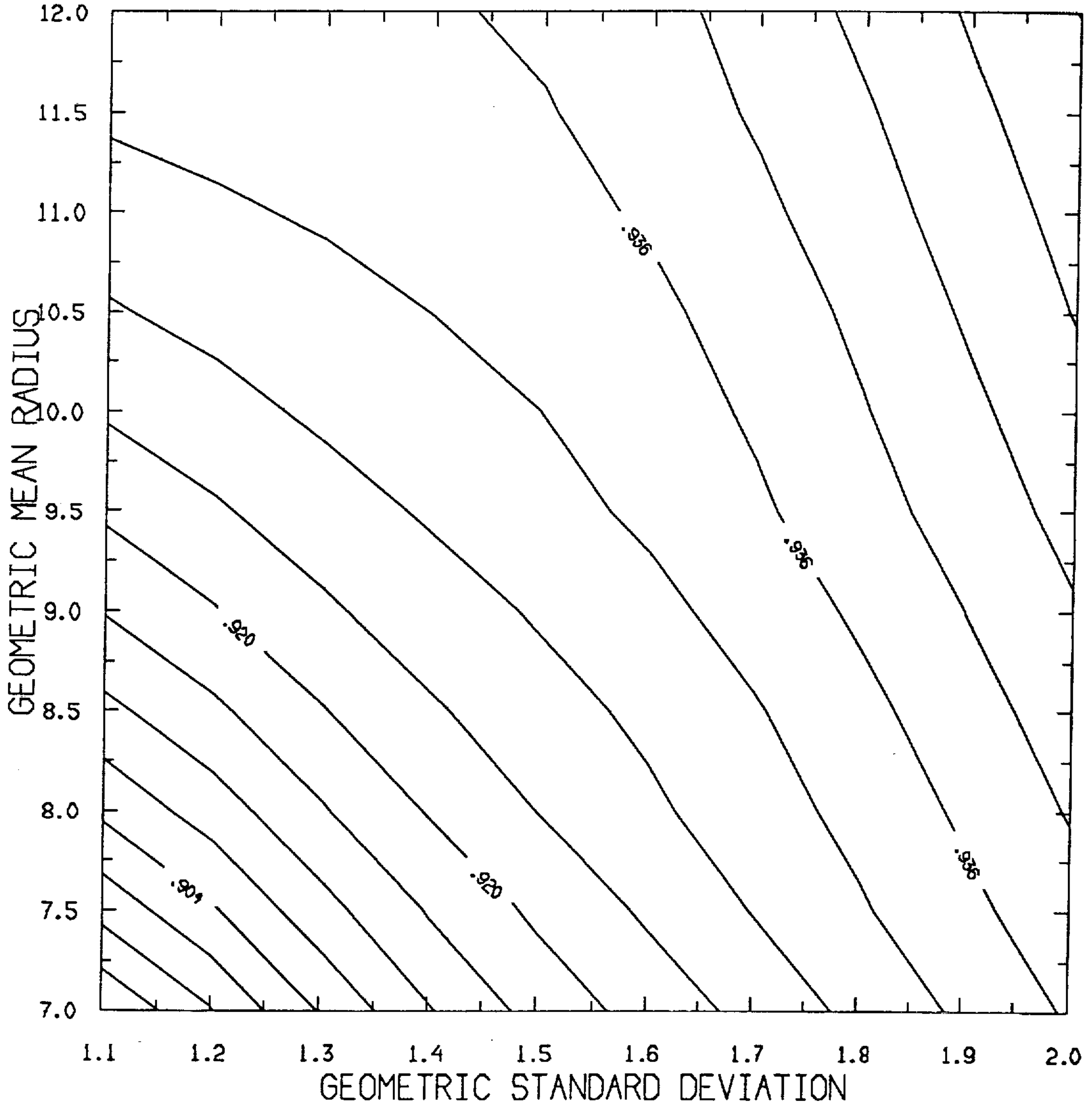

Figure (4.2.c) The contours of asymmetric factor at 10 μm as a function of the geometric mean radius and the geometric standard deviation. Contour minimum: 0.888; maximum: 0.952; increment between two contours: 0.004.

$$F = \Gamma k_1 e^{\varepsilon\tau} + k_2 e^{-\varepsilon\tau} + C^- \qquad (4.3),$$

where F = upward flux,

F = downward flux,

$C^+ = C^- = 2\pi\mu_1 B(T_c)$,

$\mu_1 = 1/2$,

T_c = cloud temperature,

$B(T_c)$ = plank function at temperature T_c,

$\varepsilon = (\gamma_1^2 - \gamma_2^2)^{1/2}$,

$\Gamma = \gamma_2 / (\gamma_1 + \varepsilon)$,

$\gamma_1 = 2 - \varpi_0 (1 + g)$,

$\gamma_2 = \varpi_0 (1 - g)$.

The boundary conditions are substituted into (4.1) and (4.2) to obtain k_1 and k_2:

$$F(\tau = 0) = 0,$$

$$F(\tau = \tau_c) = \pi B(T_s),$$

where τ_c is the IR optical depth of the cloud, and T_s is the surface temperature.

4.1.3 The Flux Extrapolation Scheme

The purpose of this scheme is to extrapolate the reflectivity at the cloud top to some distance above the cloud deck. The observed albedo data was acquired when the aircraft was around 500 m above the cloud. We have to consider the extrapolation because the horizontal variability in reflected flux at the cloud top.

In this scheme, first, we assumed that clouds are diffuse reflectors. That is to say the intensity reflected is isotropic. Therefore, $F(x,y,z_0) = \pi I(x,y,z_0)$. However, the intensity at $z = z_0 + \Delta z$ (where Δz is some incremental height above the cloud top) is not isotropic,$I(x, y, z_0 + \Delta z; \Theta, \phi)$. The flux at $z = z_0 + \Delta z$ is then equal to

$$F(x,y,z_0 + \Delta z) = \iint(x,y,z_0 + \Delta z;\ \Theta,\phi) \cos\Theta \sin\Theta \, d\Theta \, d\phi \qquad (4.4).$$

We have assumed that no scattering and absorption occur within the Δz atmosphere column above the cloud. There are two ways to solve this integral. The first is more mathematical.

$$F(x,y,z_0 + \Delta z) = \int\int I((x'-x),y,z_0)\Delta z \frac{((x'-x)^2+y^2)^{1/2}}{((x'-x)^2+y^2+\Delta z^2)} \frac{\partial(\Theta,\phi)}{\partial(x',y)} \, dx' \, dy \qquad (4.5).$$

See Figure 4.3 for illustration. This is only a change of variables for the double integrals by using the Jacobian factor. The Jacobian $\frac{\partial(\Theta,\phi)}{\partial(x',y)}$ is simply equal to $\frac{\partial\Theta}{\partial x'}\frac{\partial\phi}{\partial y} - \frac{\partial\Theta}{\partial y}\frac{\partial\phi}{\partial x'}$.

Thus we can rewrite equation (4.5) as:

$$F(x,y,z_0 + \Delta z) = \int\int I(x',y,z_0) \frac{\Delta z^2}{((x'-x)^2+y^2+z^2)} dx' \, dy \qquad (4.6).$$

The second derivation contains more physics. We can rewrite (4.4) as:

$$F(x, y,z_0 + \Delta z) = \int I(\Omega) \cos\Theta \, d\Omega \qquad (4.7),$$

because $d\Omega = \sin\Theta \, d\Theta \, d\phi$. Since a horizontal surface element $dA = dx' \, dy$, on the $z = z_0$ plane subtends a solid angle $d\Omega = \frac{dA_{ortho}}{r^2}$, where dA_{ortho} is the projection of dA orthogonal to the direction **r**, (4.7) becomes:

$$F(x,y,z_0 + \Delta z) = \int I(x',y,z_0) \cos\Theta \frac{dA_{ortho}}{r^2} \qquad (4.8).$$

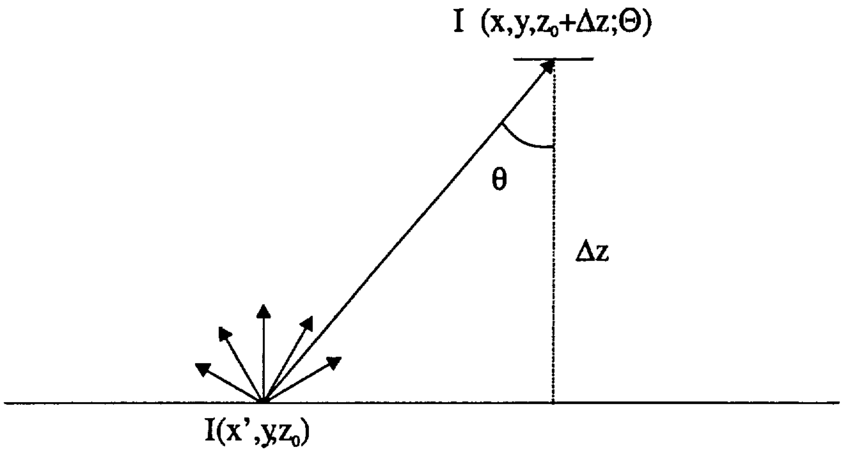

Figure (4.3) A schematic diagram of the geometry of the radiance at cloud top and the radiance at Δz above the cloud.

Furthermore, because $dA_{ortho} = \cos \Theta \, dA$,

$$F(x,y,z_0 + \Delta z) = \int\int \frac{I(x',y,z_0)\cos^2 \Theta}{r^2} \, dx' \, dy \qquad (4.9).$$

By substituting $\cos \Theta = \frac{\Delta z}{r}$, and $r = ((x'-x)^2 + y^2 + \Delta z^2)^{1/2}$, equation (4.9) eventually becomes (4.6).

Moreover, in our simulations, the intensity at the cloud top is constant with respect to y, because cloud geometry does not vary in y direction. (See section 4.2 for detailed descriptions.) Equation 4.6 can be further simplified into:

$$F(x,y,z + \Delta z) = \int I(x',z_0) \, \{\int \frac{\Delta z^2}{[y^2 + ((x'-x)^2 + \Delta z)^2]} \, dy\} \, dx'$$

$$= \int \frac{1}{2} \pi \, I(x',z_0) \frac{\Delta z^2}{[(x'-x)^2 + \Delta z^2]^{3/2}} \, dx'$$

$$= \frac{F_0}{2} \int R(x',z_0) \frac{\Delta z^2}{[(x'-x)^2 + \Delta z^2]^{3/2}} \, dx'$$

$$= \frac{F_0}{2} \Sigma R(x_i,z_0) \frac{\Delta z^2}{[(x_i - x)^2 + \Delta z^2]^{3/2}} \, \Delta x \quad (4.10),$$

where F_0 = incident solar flux on cloud, $R(x_i,z_0)$ = the reflectivity at (x_i,z_0). Equation (4.10) is the equation we use to convert the reflectivity at the cloud top calculated by the Monte Carlo method into an upward flux at 500 m above the cloud top.

The upper limit of Δx for the convergence of (4.10) has been carefully examined. We use an infinite homogeneous cloud deck of which the reflectivity is constant in space as our first-step approach to the convergence problem. It is found that when $\Delta z = 500m$, 200m is the upper limit of Δx. Therefore, the size of the photon collecting boxes could not exceed 200m in width in our simulations.

From another perspective, $\frac{\Delta z^2}{2[(x_i - x)^2 + \Delta z^2]^{3/2}}\Delta x$ serves as a weighting factor of the reflectivity at $R(x_i,z_0)$ for the calculation of $F(x,y,z_0 + \Delta z)$. Let's see the situation when $\Delta z = 500$ m and $\Delta x = 200$ m. When $(x_i\text{-}x)$ is equal to zero, the weighting factor is 0.2; when $(x_i\text{-}x)$ is equal to 1 km, the weighting factor drops to 0.018; and when $(x_i\text{-}x)$ is equal to 5 km, the weighting factor further decreases into 0.0002. Furthermore, we have estimated that if the intensity were isotropic, about 90 % of the measured flux would be contributed by reflected intensities from cloud top within a width of 1.1 km around the aircraft which is at a height of 500 m above cloud top.

4.2 Simulations by the Monte Carlo Method

From the satellite image (Figure 3.1), we can see that the clouds along the path that the airplane flew are of the cloud-street type. Thus, in our simulations, the x axis is defined as the flight path. We assumed that the clouds extend to infinity in the y direction, and the geometry and cloud optical properties are only functions of x. That is to say, the unit cell (defined in Section 2.3.1) is an infinite cloud strip extending along y axis. As a result, the reflectivity at the cloud top remains invariant in the y direction. Because of this simplification, we need only collect outgoing photons along the x axis when they leave the cloud.

Table 4.1 lists all the constants necessary to be specified in order to execute the simulations and the values that we choose.

The incident solar zenith angle Θ_0 and the incident solar azimuth ϕ_0 are calculated by the following equations (Spencer, 1971):

	Symbols	Descriptions	Values
Incident angles	Θ_0	Incident zenithal angle	165°
	ϕ_0	Incident azimuthal angle	90° or 0°
Cloud geometry	H	Cloud depth	260 m
	W_h	Width of the hole at cloud bottom	1 km
	W_c	Width of the cloud at cloud bottom	26.1 km
Optical properties	g	Asymmetry factor	0.86
	ϖ_0	Single scattering albedo	1
	$b_{ext, \lambda=0.6\,\mu m}$	Volume extinction coefficient	$0.06154\ m^{-1*}$
	l_0	Mean free path	16.25 m
Box width	Δx	Width of a photon collecting box	200 m
Surface albedo	A_s		0

Table (4.1) The list of all the constants in the simulations and their values . *In experiment 3 and 4, the volume extinction coefficient decreases linearly, or quadratically from 0.06154 at the cloud center to 0 at cloud edges.

$$\cos \Theta_0 = \sin \theta \sin \delta + \cos \theta \cos \delta \cos h \qquad (4.11), \text{ and}$$

$$\sin \phi_0 = -\cos \delta \sin h / \sin \Theta_0 \qquad (4.12).$$

In the above two formulae, θ is latitude.

$$\delta \text{ (in radian)} = 0.006918 + 0.399923 \cos \varphi_0 + 0.070257 \sin \varphi_0 - 0.006758 \cos 2\varphi_0 + 0.000907 \sin \varphi_0 - 0.002697 \cos \varphi_0 + 0.001480 \sin 3\varphi_0 \qquad (4.13)$$

($\varphi_0 = 2\pi d_n / 365$, d_n is the day number ranging form 0 on January 1 to 364 on December 31), and h is the hour angle, which is symmetrical about solar noon in terms of the local apparent time.

$$\text{local apparent time} = \text{clock time} + \text{longitude correction} + 0.000075 + 0.001868 \cos(\varphi_0) - 0.032077 \sin(\varphi_0) - 0.014615 \cos(2\varphi_0) - 0.04849 \sin(2\varphi_0) \qquad (4.14)$$

However, we did not use the ϕ = 295° (0° is south, and the angle rotates counterclockwise), calculated according to Spencer's formulae. The reason is that there is too much uncertainty embedded in calculating the incident azimuth angle given our arbitrary coordinate system. Instead of using an uncertain azimuth angle, we decide to input photons at ϕ_0 = 90° and 0° (0° points to the positive x direction, 90° points the positive y direction and so on) for the incident azimuth angle in our simulations. In the case of 90° azimuth angle, the vertical cloud side effect should be the smallest, and at 0° it should be the largest.

H, W_h and W_c are obtained by averaging leg 5 data. However, the ceiling height was determined by another earlier flight.

Section 4.1.1 has already discussed the values for g and ϖ_0. Instead of averaging the microphysics data to acquire $b_{ext,\lambda}$ at visible wavelengths, the $b_{ext,\lambda=0.6\mu m}$ was estimated from the reflectivity data. From the Monte Carlo code for homogeneous clouds, we found that the optical depth is around 16 for clouds of reflectivity 0.55, which is the mean value of reflectivity around cloud center (Figure 3.5). We then divided cloud depth (260 m) by the optical depth 16 to get the mean free path. Discussions about this simplification is in Section 4.3.

The upper limit for the convergence of our flux extrapolation scheme, 200m, is used as the width of the photon collecting boxes. The ocean is assumed to be black in the visible wavelengths. In fact, this assumption is reasonable (Figure 4.4) since the zenith angle is small in this case.

Table (4.2) summarizes the four simulations we conduct. Experiment 1, in which the geometry effect is minimum and b_{ext} is constant, serves as the control mode of the simulations. In experiment 2, the cloud geometry effect is a maximum. In this run, the cloud geometry is most similar to the cloud top height data. Experiment 3 and 4 investigate the effects of a variation of b_{ext} on reflectivity with small cloud geometry effect. Figure (4.5) displays the three kinds of cloud shapes used here in comparison with the cloud top data of leg 5.

In experiment 3 and 4, because of our simplification of tracking photons through a b_{ext} varying medium (Section 2.3.1), one potential problem rises when photons collide with cloud droplets near cloud edges. At the edge of cloud, the mean free path ($1 / b_{ext}$) will increase drastically; therefore, we will overestimate free paths (Equation 2.12).

4.3 Results

Figure (4.6) shows the results of the four simulations. The azimuth direction of the incident photons points to the positive x direction in each case.

As it is shown on the plot, the results of simulation 1 and simulation 2 are similar, even though the reflectivity of simulation 1 varies slightly sharper in the vicinity of the cloud edge. This is not a surprising result, because, from Figure (2.7), the cumulative

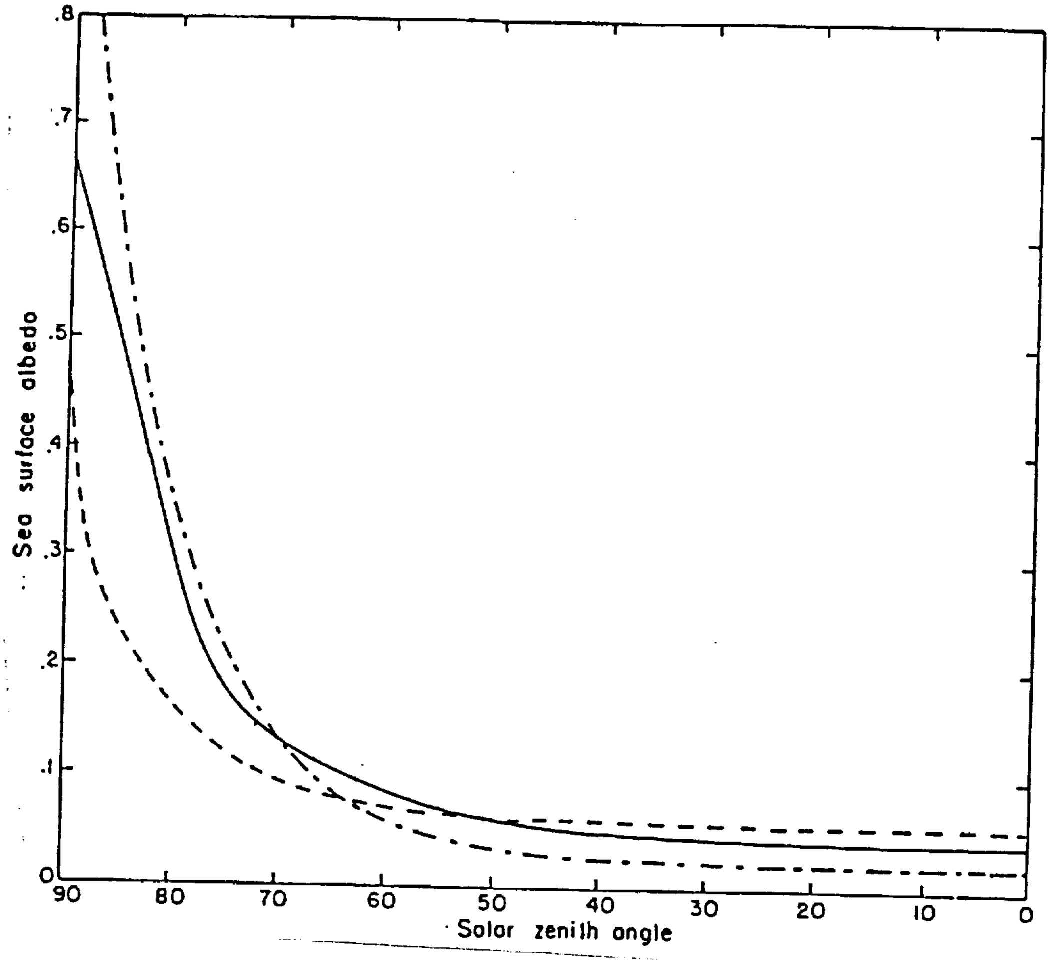

Figure (4.4) The albedo of the ocean surface as a function of the solar zenith angle and the vertical transmissivity of the atmosphere: ——, clear (transmissivity 0.6-0.65); -----, thin overcast (transmissivity 0.35 -0.4), -·--·-, computed for a parallel beam and a smooth surface. Courtesy (Kondratyev, 1969)

#	Cloud shape	Descriptions	b_{ext}	Descriptions
1	Rectangular	Rectangular cloud blocks	Constant	
2	Trapezoidal	Trapozoidal cloud blocks with a width of 26.1 km at bottom and a width of 22.1 km at top	Constant	
3	With rounded edge	Cloud edge is rounded with a radius of 260 m	Linear variation	b_{ext} decreases linearly from 0.06154 m^{-1} to 0 from cloud center to cloud edge
4	With rounded edge	The same as experiment 3	Quadratic variation	b_{ext} decreases quadratically from 0.06154 m^{-1} to 0 from cloud center to cloud edge

Table (4.2) Descriptions of 4 experiments.

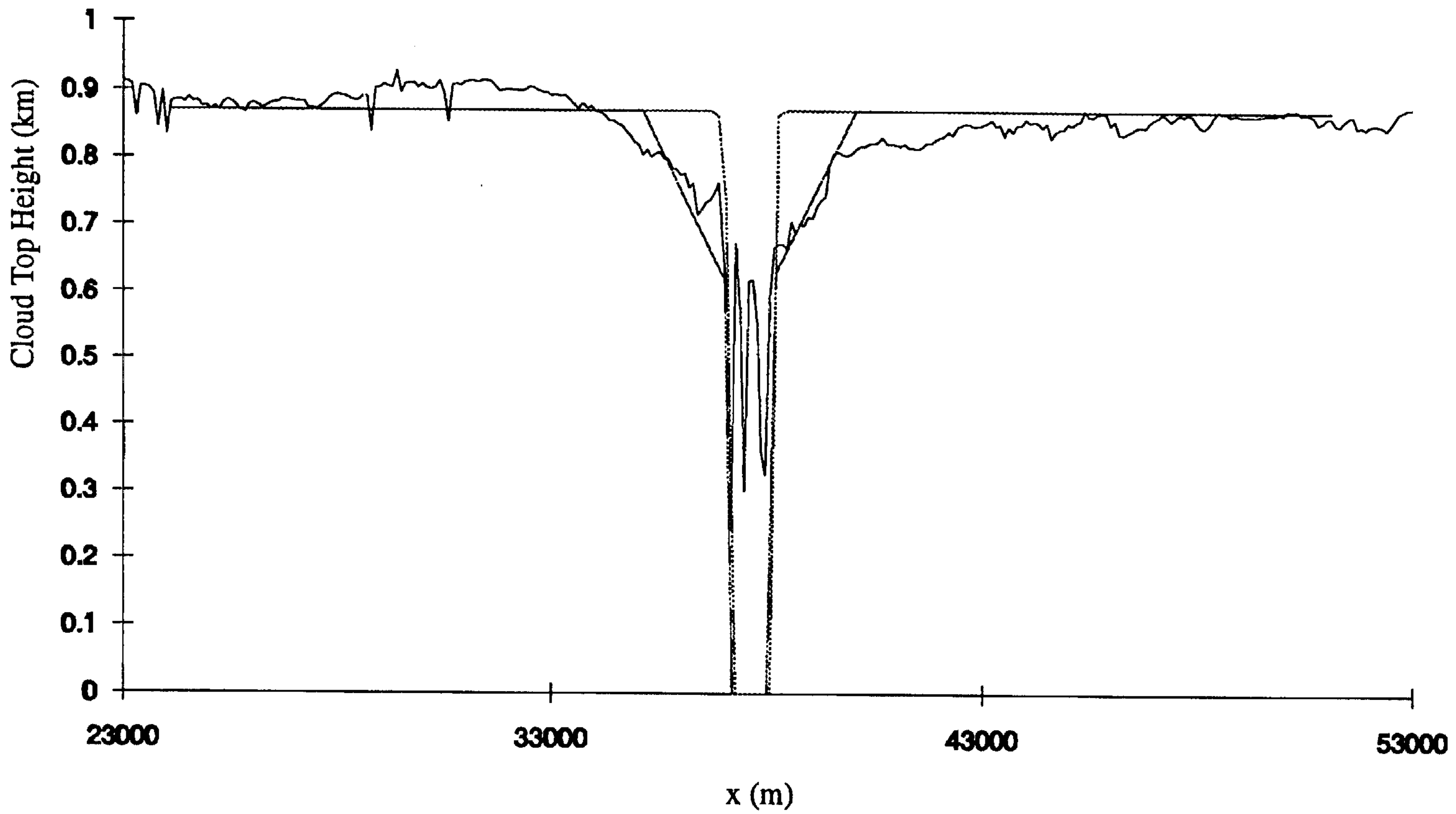

Figure (4.5) The plot of cloud top height measured by lidar and that for experiment 2, 3, 4. The cloud top height of experiment 1 is not shown; however, it is very close to that of experiment 3 and 4. The solid line for cloud top measured by lidar; the dashed line for experiment 2; the dotted line for experiment 3 and 4.

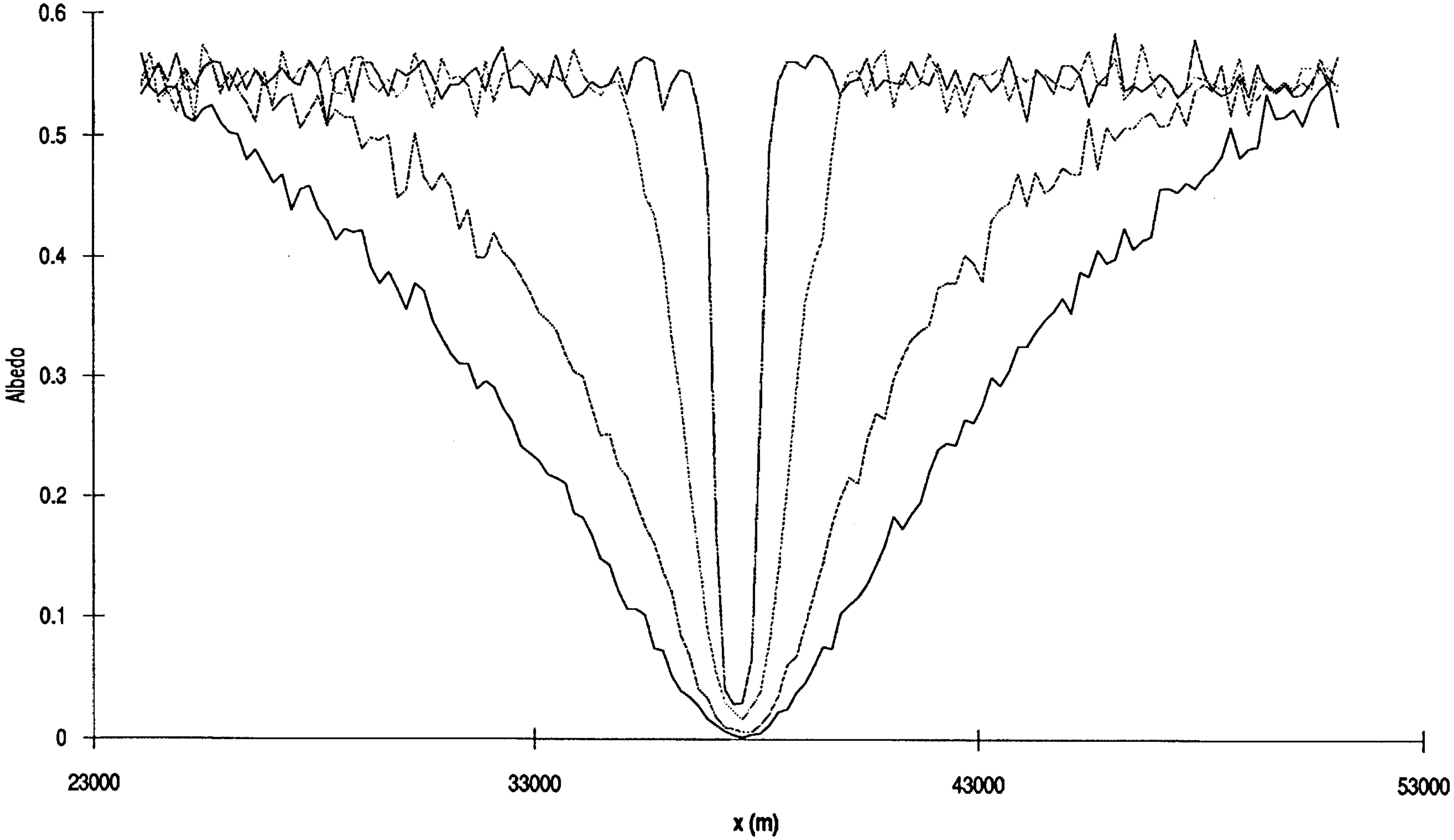

Figure (4.6) A plot of albedo for four experiments at the top of cloud. The incident azimuth angle is 0°. The dashed line denotes experiment 1; the dotted line for experiment 2; the solid line for experiment 3; and the dashed-dotted line for experiment 4.

probability density diagram in the x direction, in which the optical depth is 16, and the incident azimuth angle is 15°, shows that the probability of photons reflecting from the cloud at a distance 75 times the mean free path is very small. Thus, the geometry effect could only possibly affect the radiation field about 1 km from the starting and the ending points of the geometry variation. For example, for experiment 1, the geometry only affects the reflectivity between 36.1-39.1 km, for experiment 2, between 34.1-41.1 km.

In contrast, the results of simulation 3 and 4 show more gradual change of reflectivity from the cloud center to edge. Except near the center of the clouds where the reflectivity of experiments 3 and 4 are almost the same, the reflectivity of experiment 3 is less than that of experiment 4. This is consistent with the optical depth variation of the two experiments. (Figure 4.7)

Similar experiments were conducted to investigate the azimuth angle effects. This time, the incident azimuth angle was set to be 90°; that is to say, the incident azimuth angle is directed along the positive y direction. Figure (4.8) is a series of comparisons of two extreme incident azimuth angles for each of the four experiments. From figure 4.8, there are no obvious differences between the 90° and 180° cases. The original conjecture of these experiments was that the reflectivity of 180° incident azimuth angle would be larger than that of 90° cases at the vicinity of cloud, because the vertical sides of clouds would reflect more photons for 180° cases. However, we can not see obvious differences at the vicinity of clouds. Possible reasons are the incident zenith angle is too close to that of solar noon, and the fractional cloud coverage is near unity.

Since the difference between 90° and 0° cases is not obvious, only the 0° cases are used in the discussions below. We now apply the flux extrapolation scheme to the raw results. Figure (4.9) is a series of comparisons between the cloud-top results and the extrapolated results. From these figures, we can conclude that the flux extrapolation scheme smoothes the variability of the Monte Carlo method. Also, the reflectivity of the

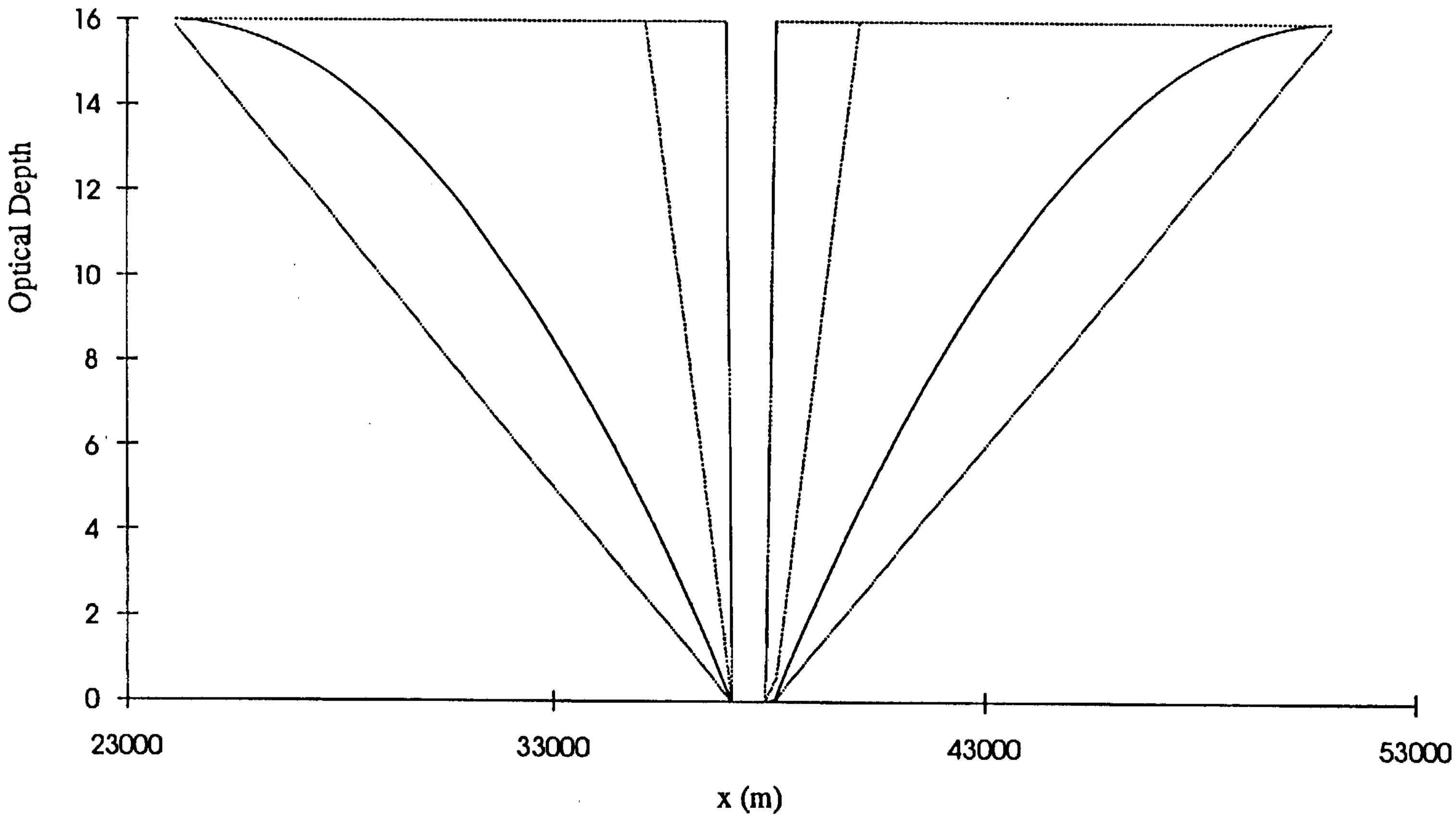

Figure (4.7) A plot of optical depth for four experiments. The dashed line denotes experiment 1; the dotted line for experiment 2; the solid line for experiment 3; and the dashed-dotted line for experiment 4.

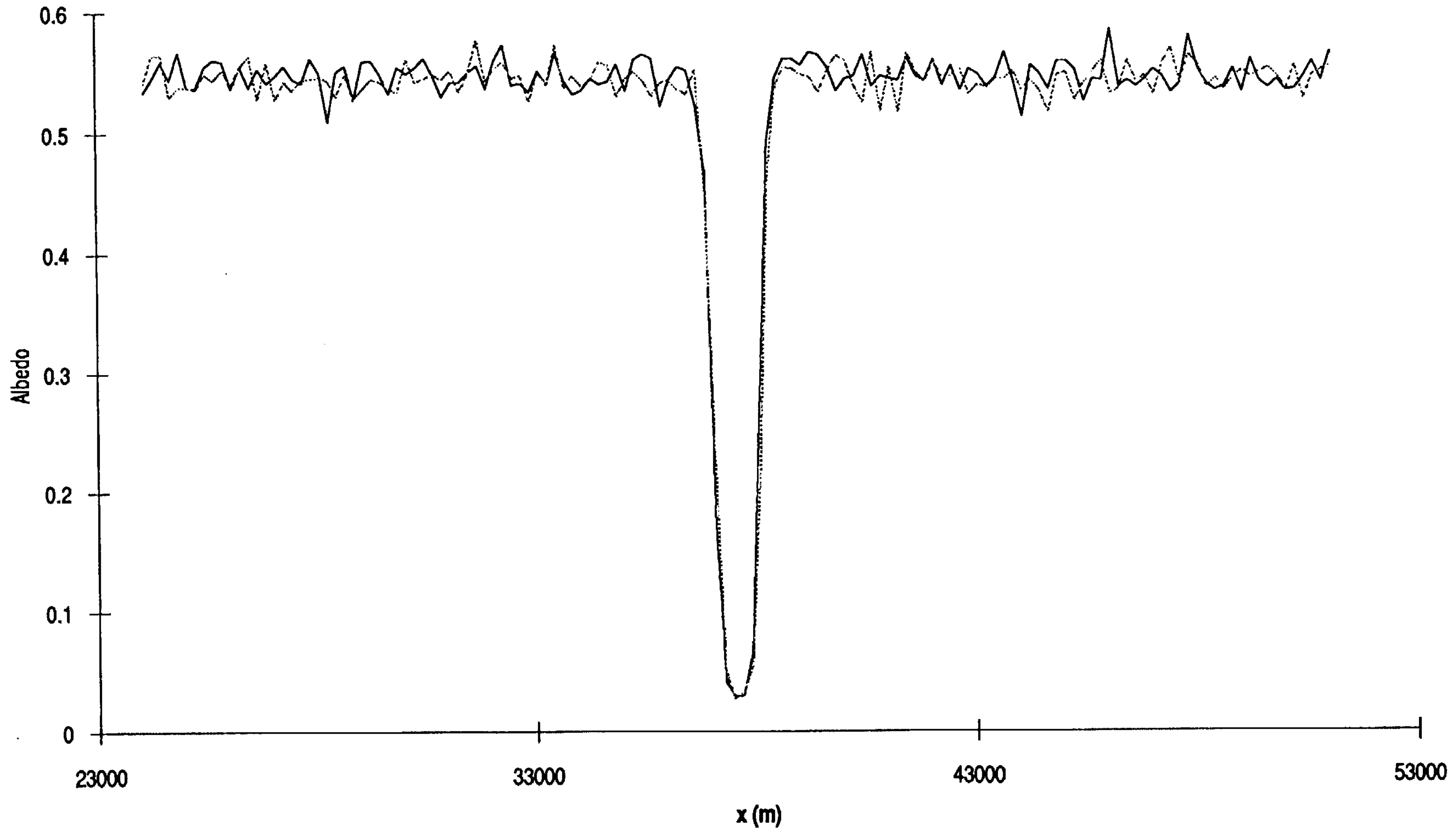

Figure (4.8.a) A comparison of albedo between 0° incident azimuth angle (the solid line) and 90° incident azimuth angle (the dotted line) for experiment 1.

FIG4-8-4.XLC

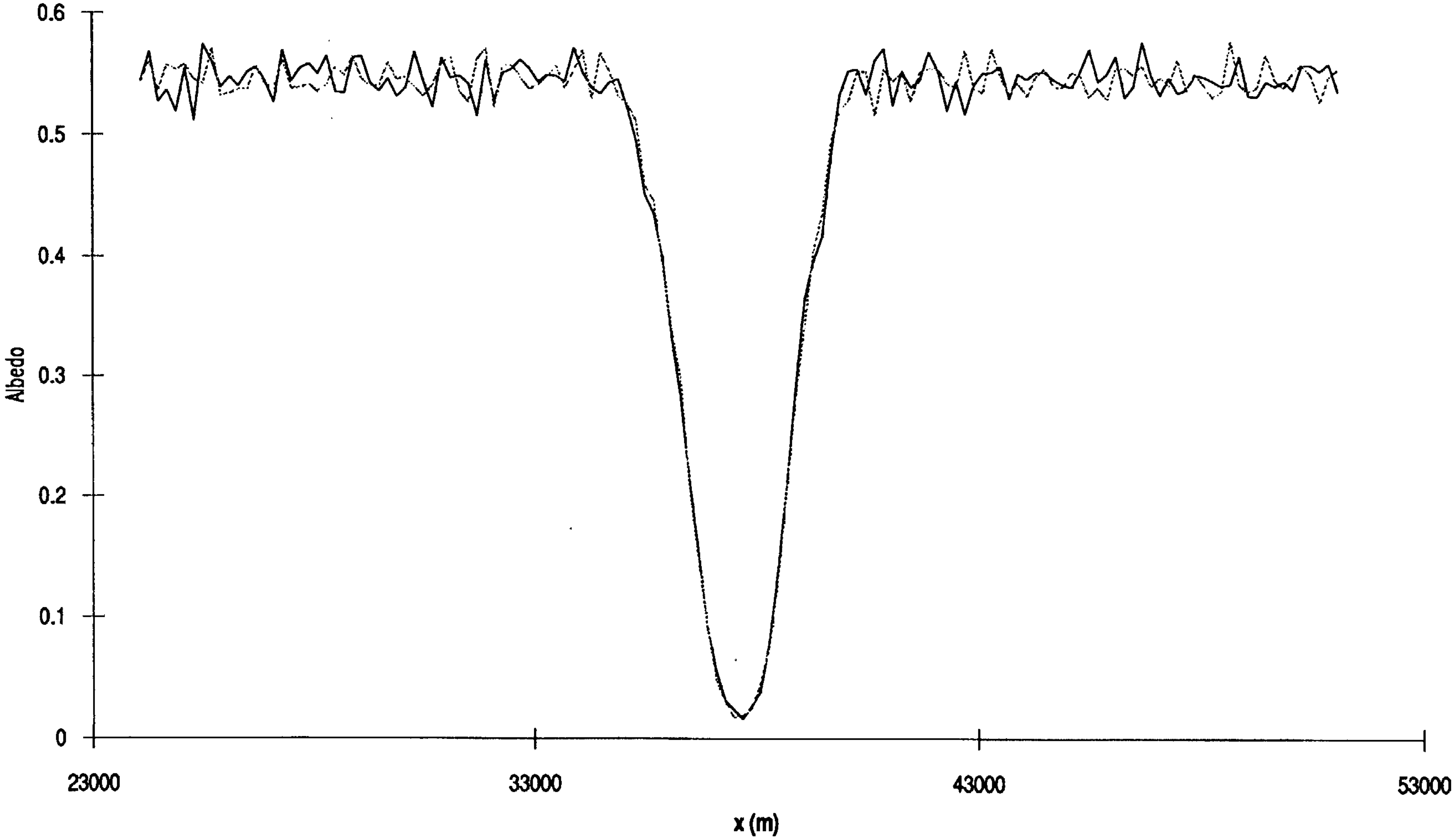

Figure (4.8.b) A comparison of albedo between 0° incident azimuth angle (the solid line) and 90° incident azimuth angle (the dotted line) for experiment 2.

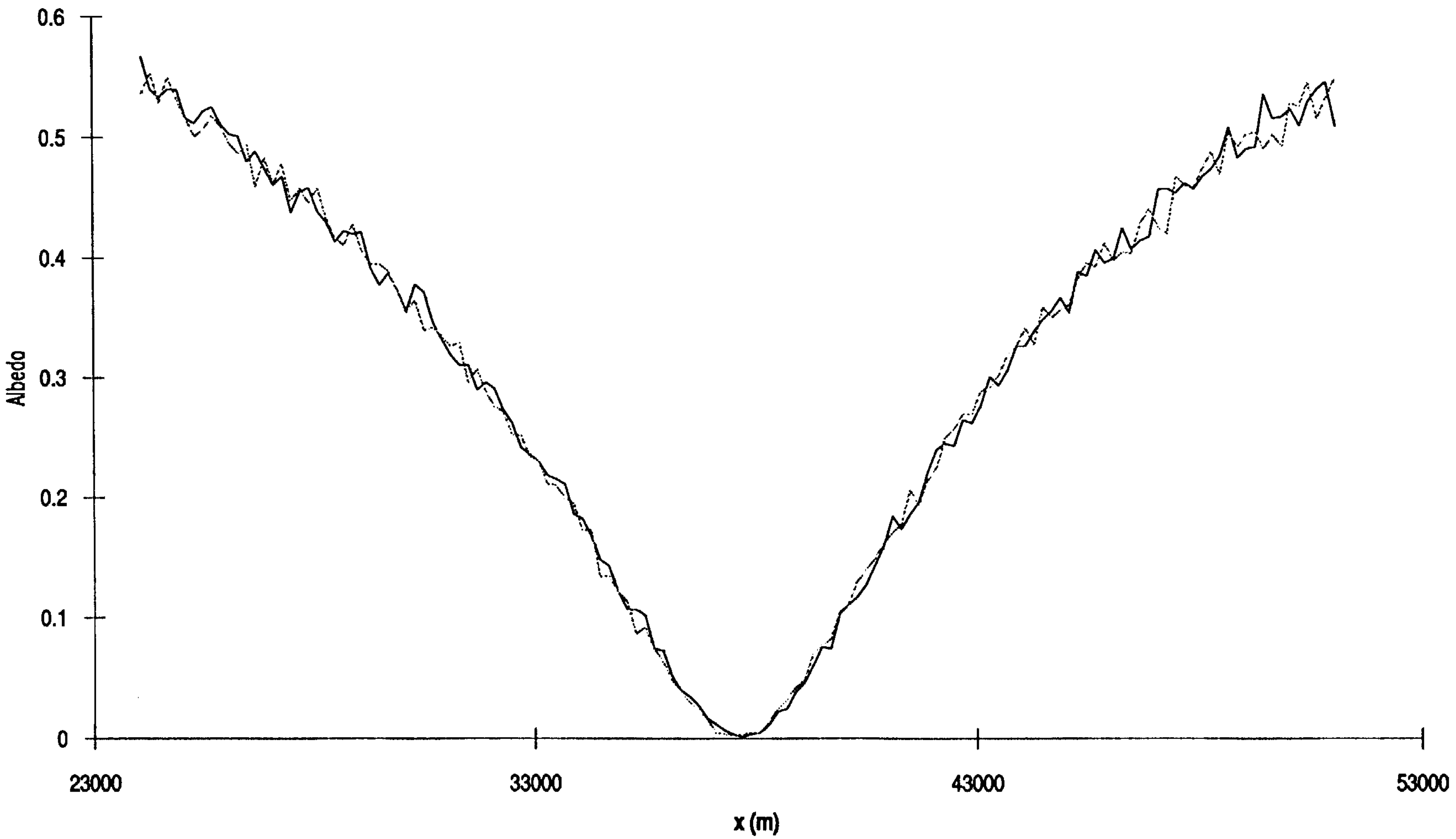

Figure (4.8.c) A comparison of albedo between 0° incident azimuth angle (the solid line) and 90° incident azimuth angle (the dotted line) for experiment 3.

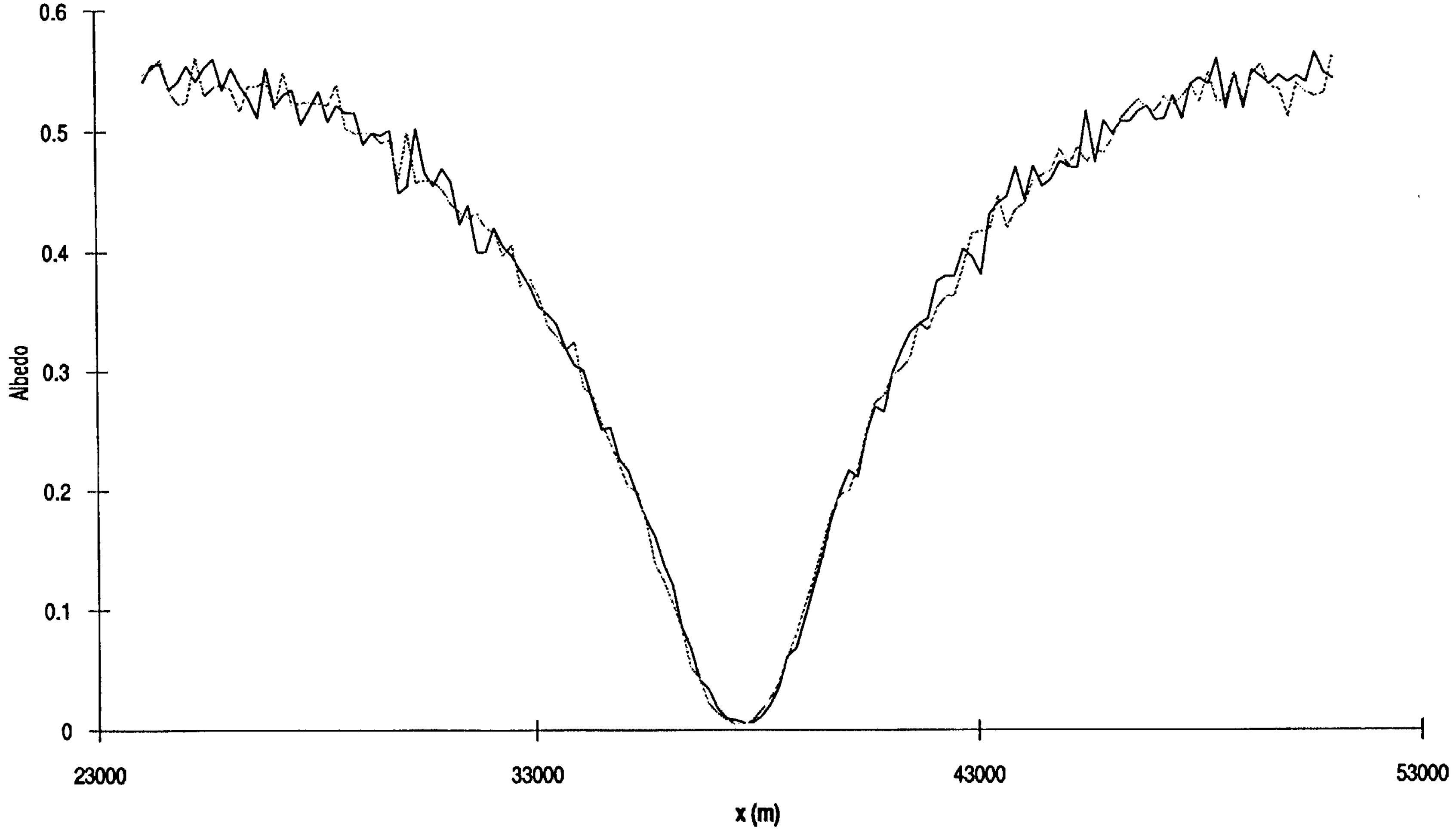

Figure (4.8.d) A comparison of albedo between 0° incident azimuth angle (the solid line) and 90° incident azimuth angle (the dotted line) for experiment 4.

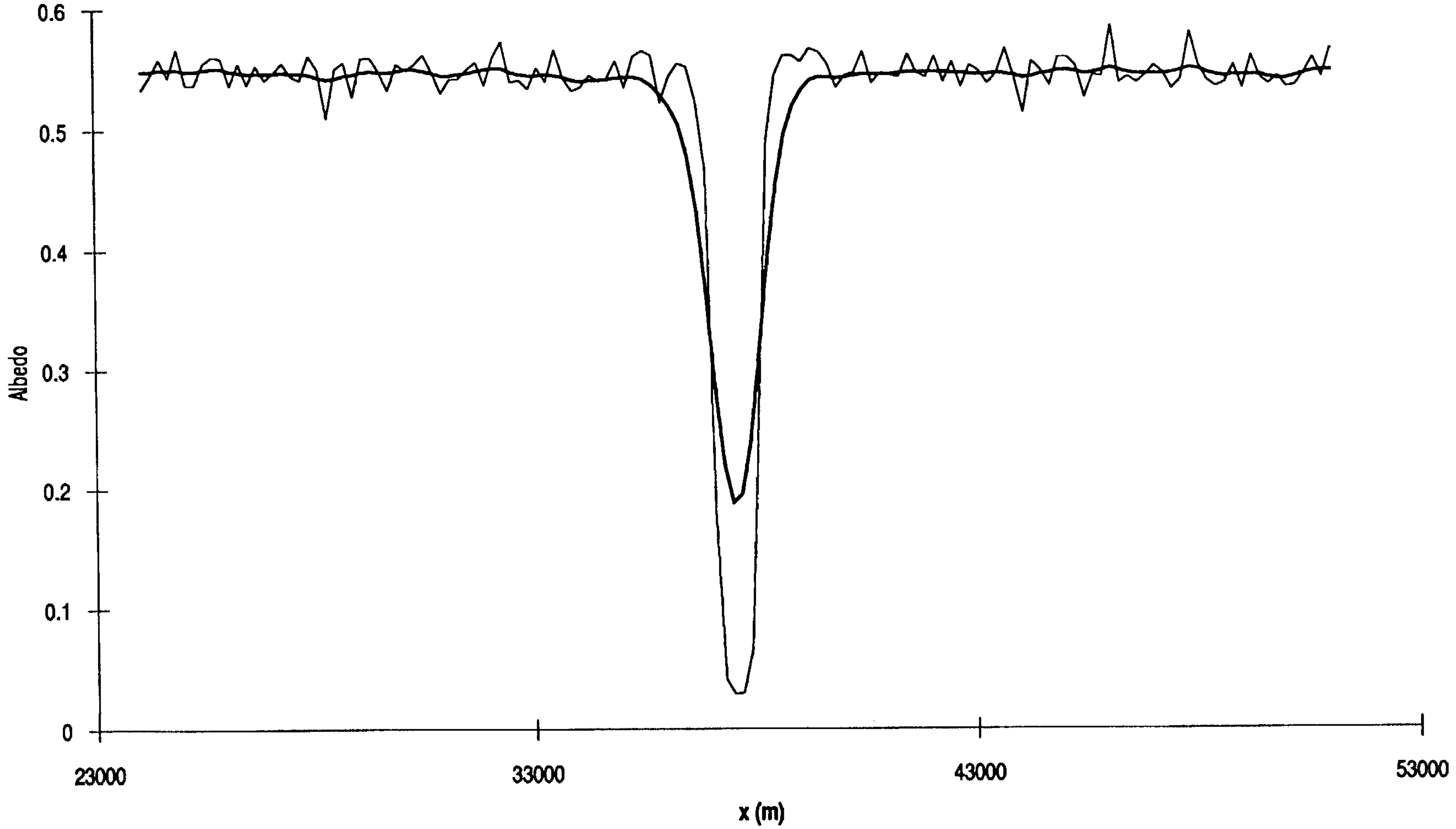

Figure (4.9.a) Albedo at the cloud top before extrapolation (the light line) and albedo after extrapolation (the heavy line). Results from experiment 1.

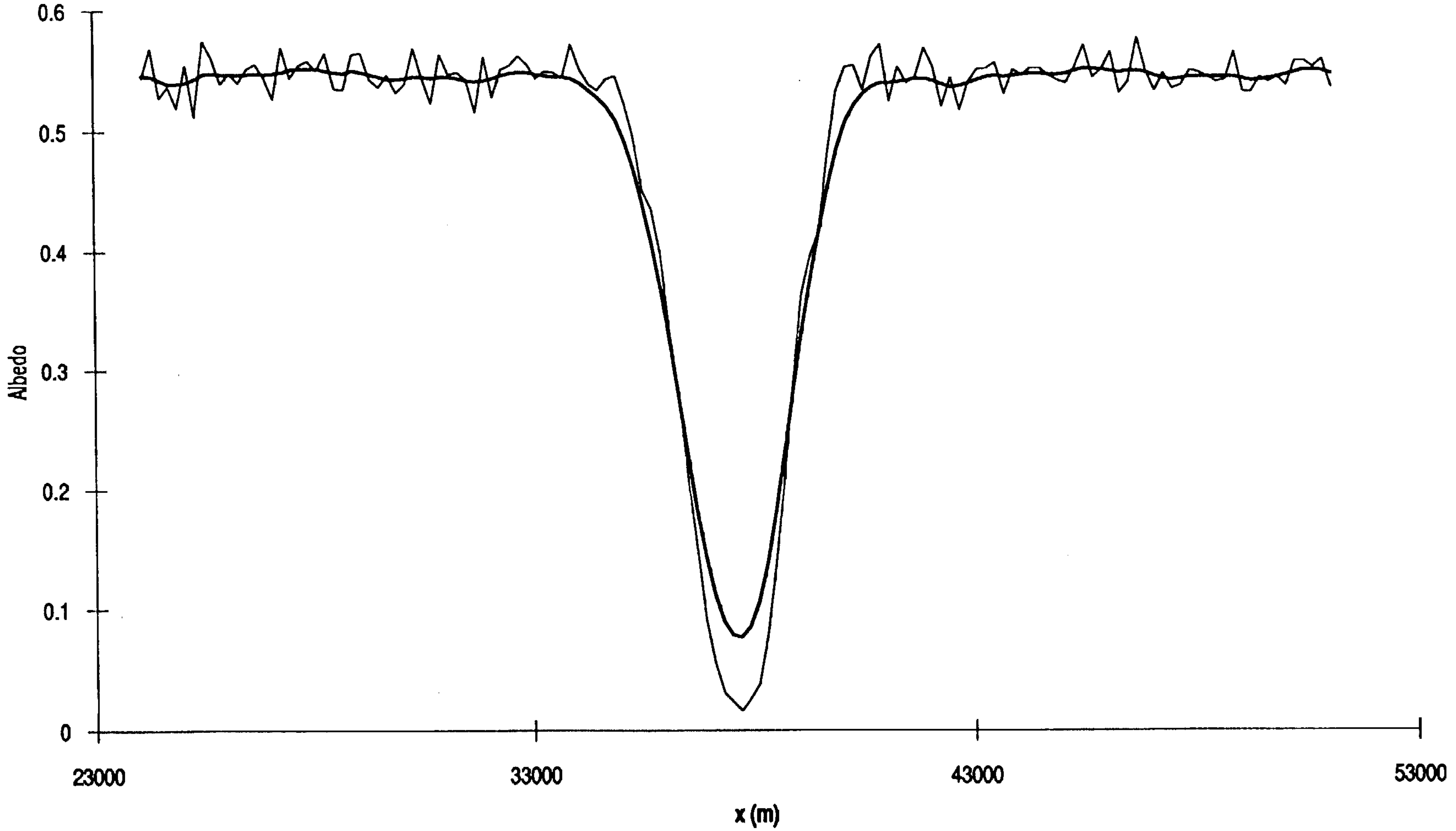

Figure (4.9.b) Albedo at the cloud top before extrapolation (the light line) and albedo after extrapolation (the heavy line). Results from experiment 2.

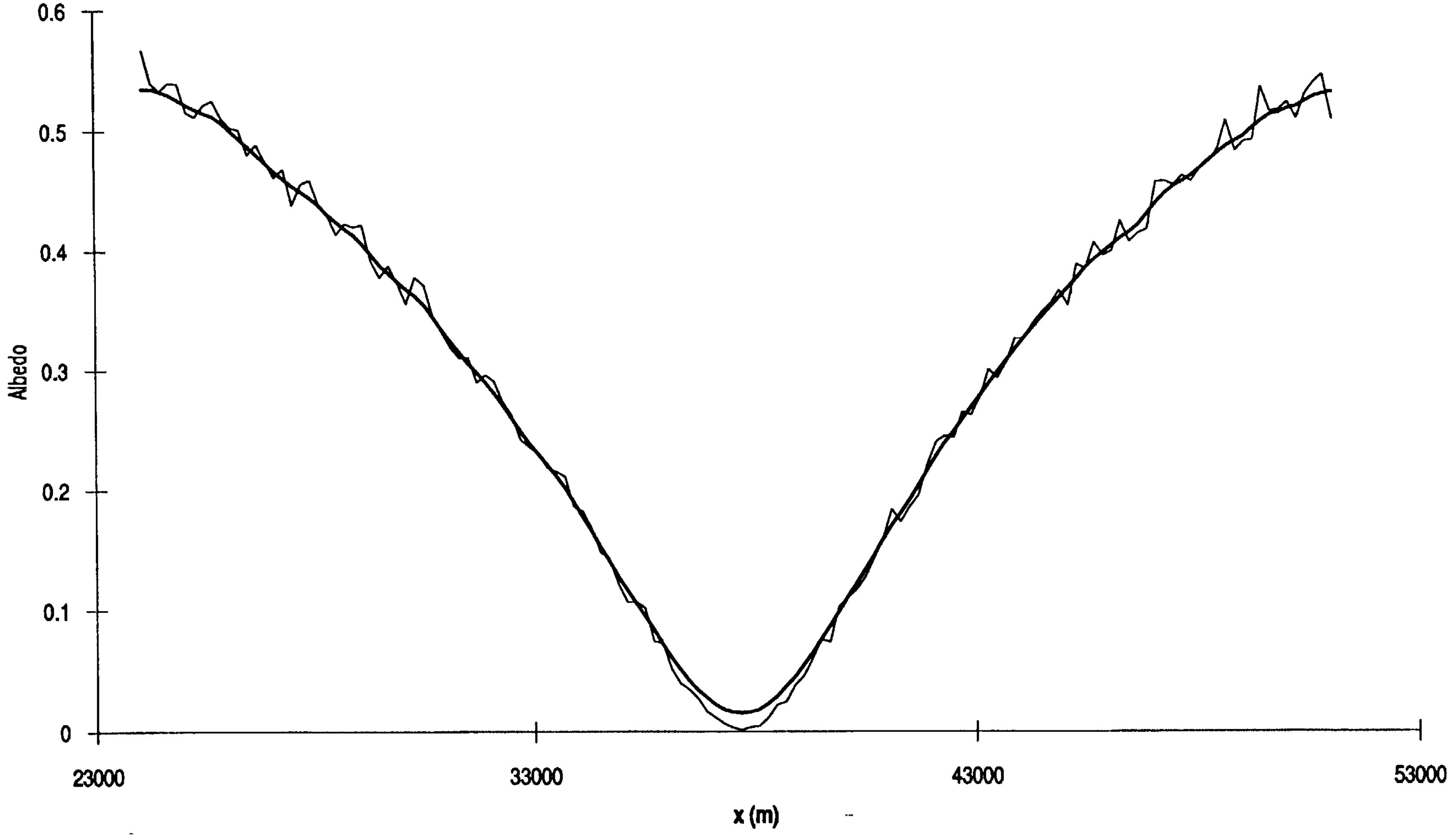

Figure (4.9.c) Albedo at the cloud top before extrapolation (the light line) and albedo after extrapolation (the heavy line). Results from experiment 3.

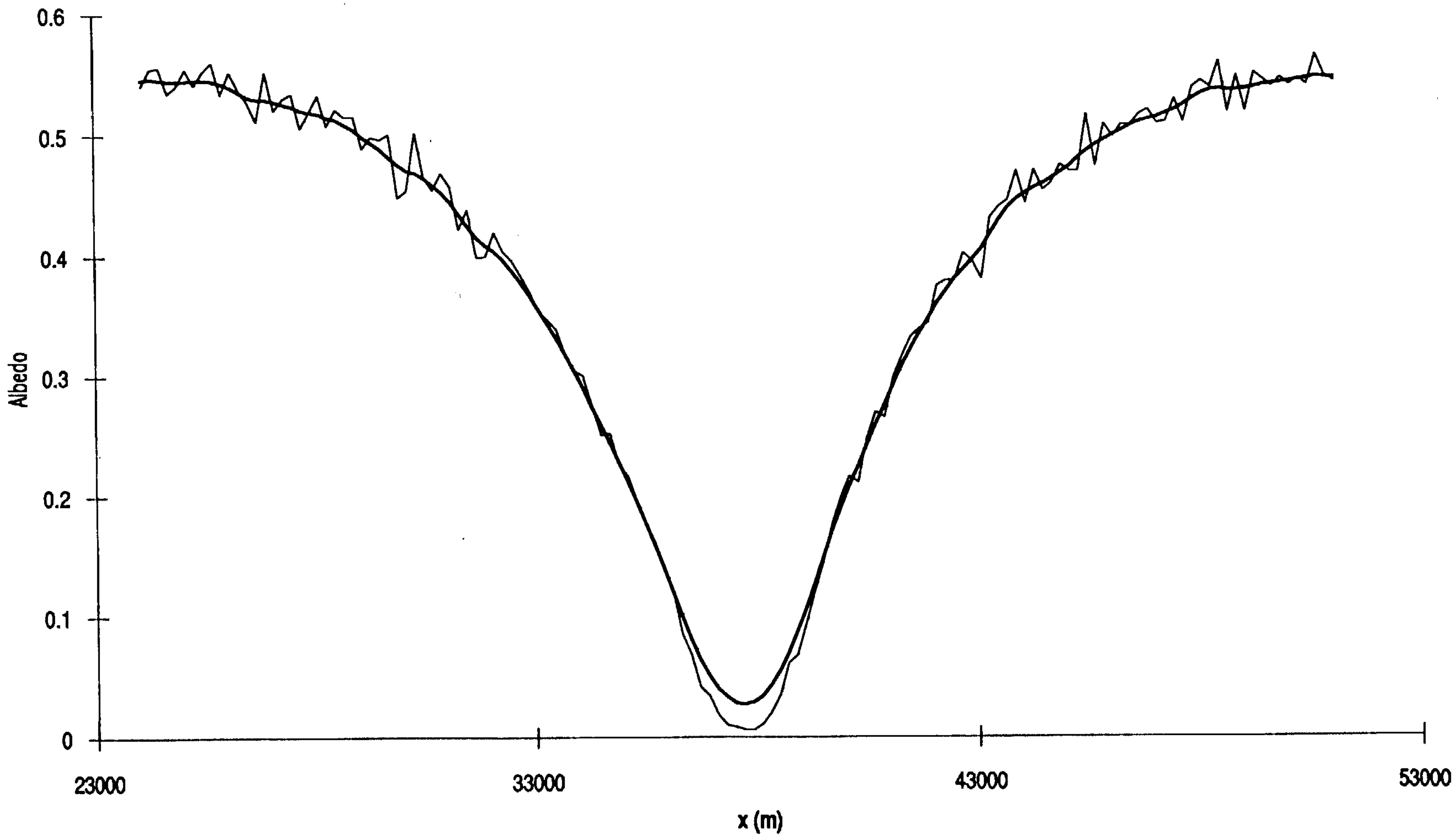

Figure (4.9.d) Albedo at the cloud top before extrapolation (the light line) and albedo after extrapolation (the heavy line). Results from experiment 4.

hole increases after extrapolation due to side effects. This is consistent with our discussion of the flux extrapolation scheme in Section (4.1.3).

We can plot these modified results with our observational data (Figure 4.10). The observed albedo matches fairly well with the experiment 4 in the left part of the cloud. At the hole, both experiment 3 and 4 underestimate the reflectivity but only with an error about 0.05, which is close the 5 % sea surface reflectivity for small azimuth angles in Figure (4.4). At the right cloud block, the observed albedo first agrees with the reflectivity calculated by experiment 4 and then it becomes smaller than that of experiment 3 with a discrepancy about 0.05 in maximum. Both experiment 1 and experiment 2 are unable to create a gradual change of reflectivity from cloud center to cloud edge. They only match the observed data well at the hole. Thus, this implies the geometry effect alone is not sufficient to result in the albedo change of observation.

Now, the IR data are used to check our results. First of all, we have to determine the g, ϖ_0 and σ_{ext} for IR at 10 μm. The log-normal distribution of cloud droplets assumed in the Mie code is checked from data (Figure 4.11). We found that the log-normal distribution assumption is good when the cloud is solid, or when the observed data is at the center of clouds. The cloud microphysical data is then used to obtain the geometric mean radius and geometric standard deviation for those sets satisfying the log-normal distribution. The points with "+" symbols in Figure (4.12) are sets of the $\overline{r_g}$ and σ_g calculated from observational data.

In section (4.3), we have mentioned that the value of the extinction coefficient in the visible is set to be 0.0654 m^{-1}. However, from the observational data, the number density of cloud droplets is around 30 to 55 per cm^3. Even if the maximum 55 per cm^3 is input for the calculation of extinction cross section:

$$\text{extinction coefficient} = \text{volume extinction cross section} * \text{number density} \qquad (4.11),$$

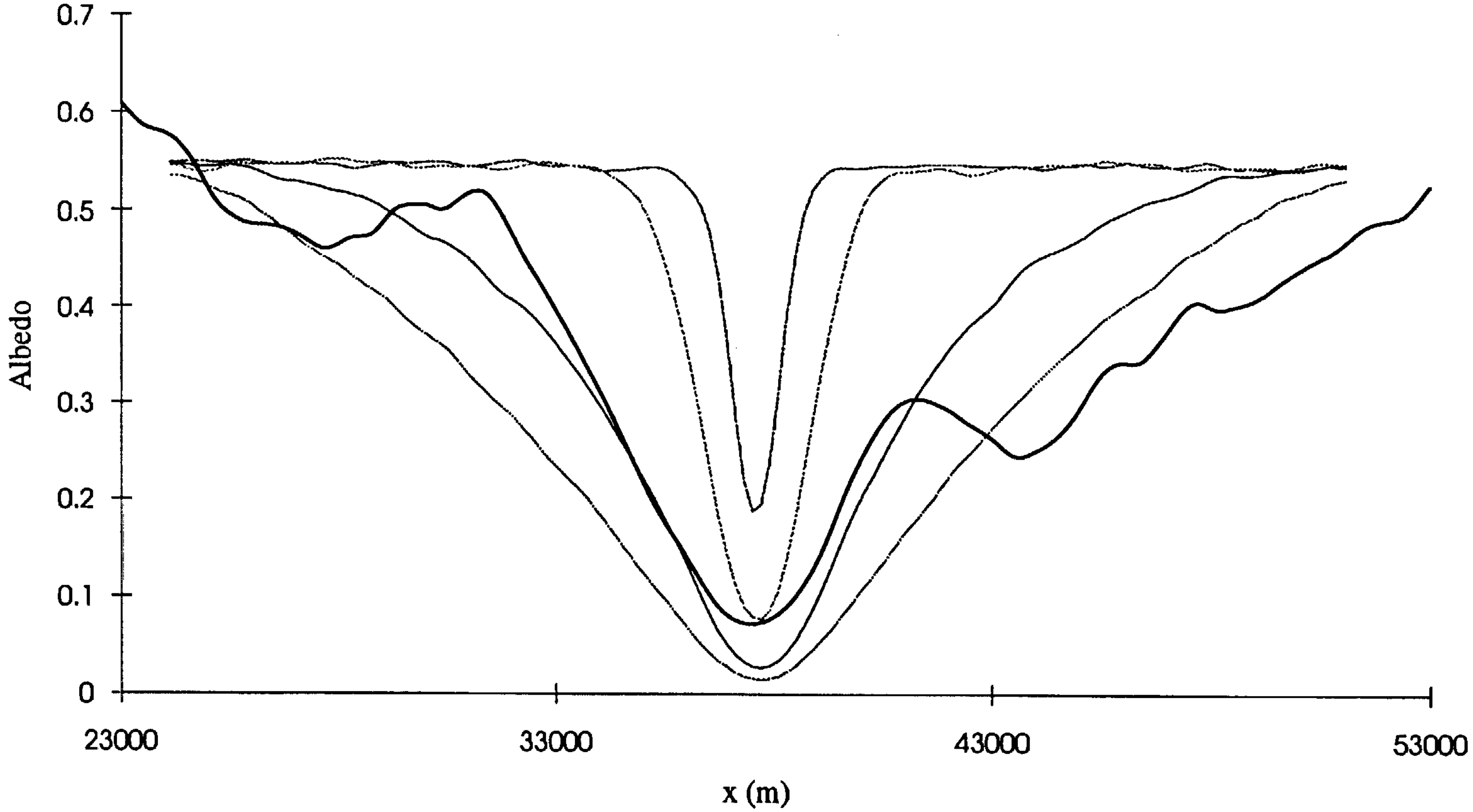

Figure (4.10) The observed albedo and simulation results along the flight path. The heavy black line denotes the observed albedo; the dashed line for experiment 1; the dotted line for experiment 2; the dash-dotted line for experiment 3; and the solid line for experiment 4.

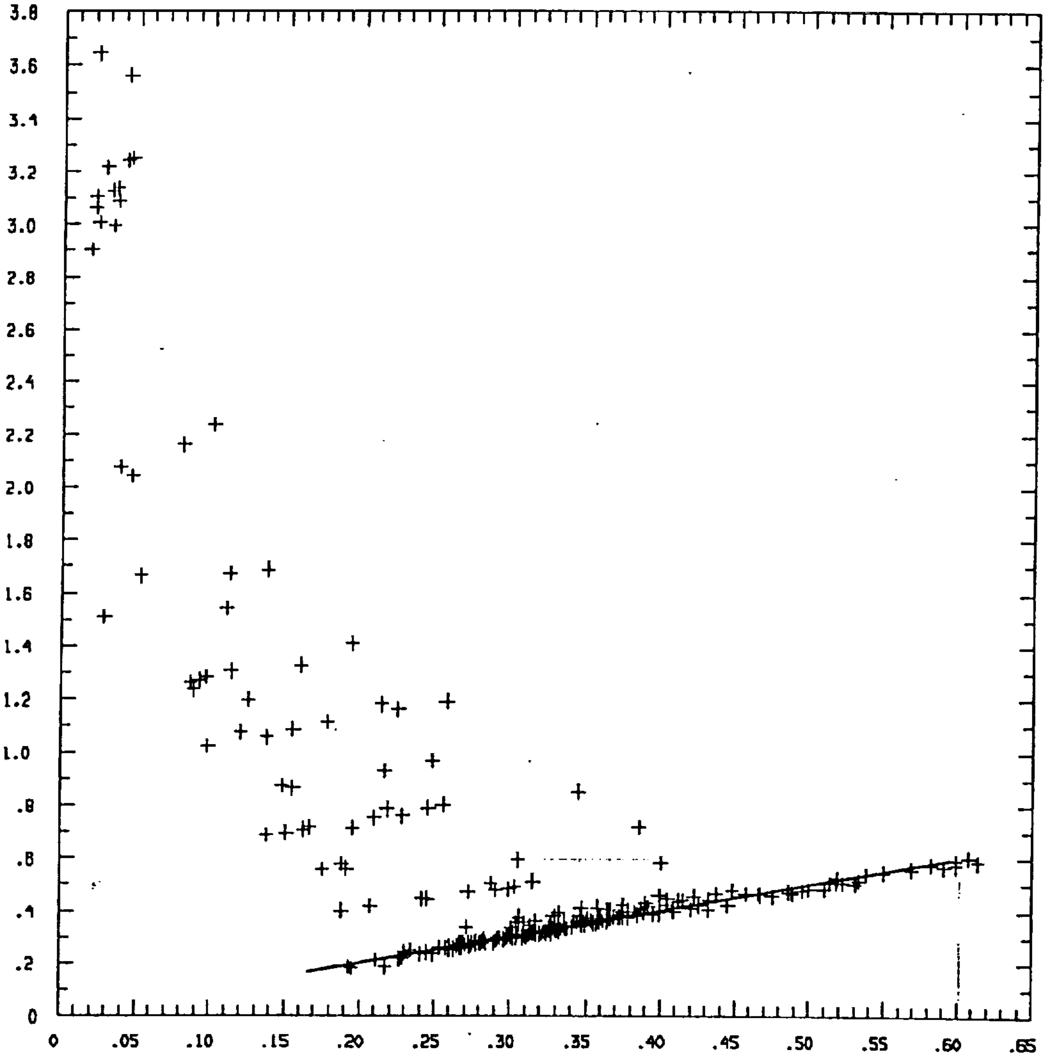

Figure (4.11) The scatter plot of the standard deviation calculated from measured LWC and $\bar{d}$ by FSSP using the log-normal cloud droplet distribution assumption (y axis) and the standard deviation measured by FSSP (x axis). The straight line denotes cases that perfect matches of the two standard deviations take place.

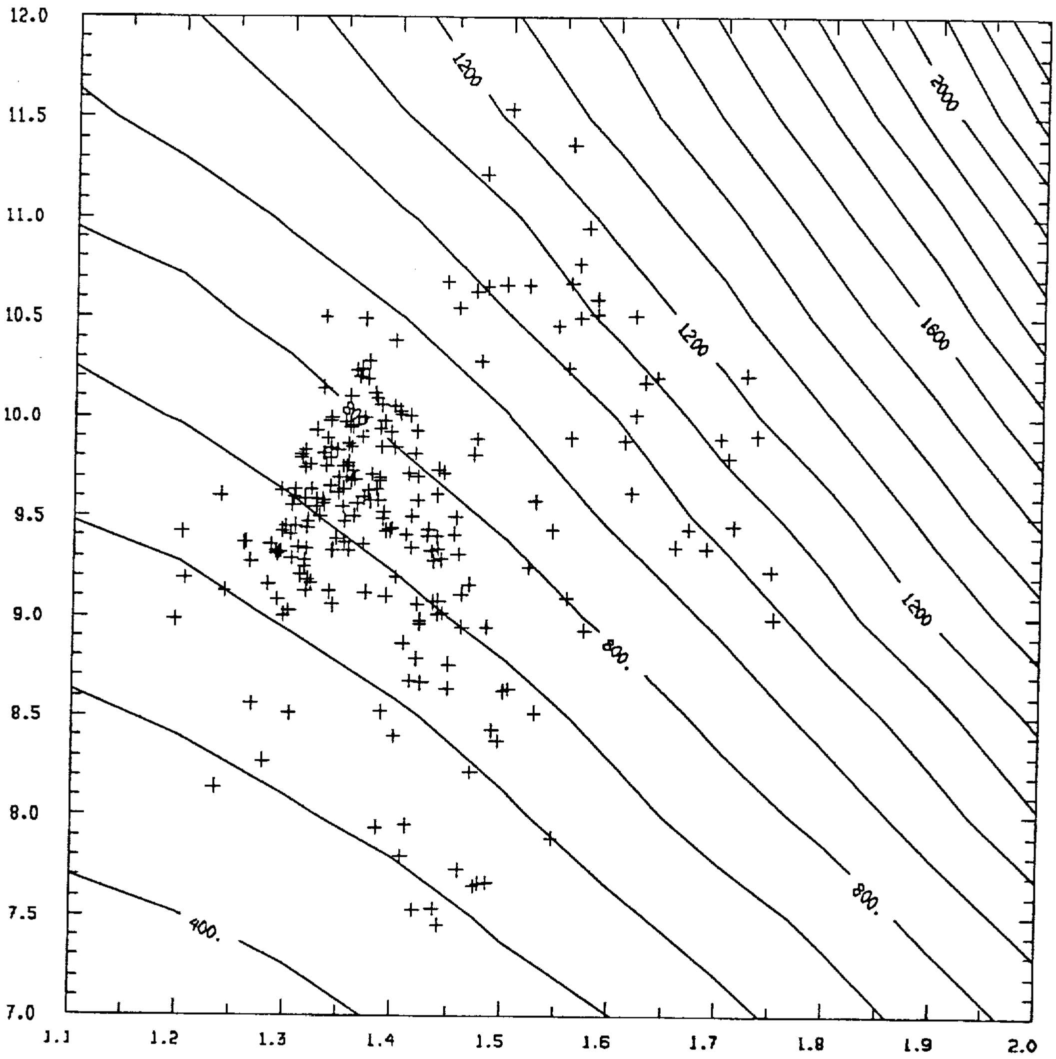

Figure (4.12) The scatter plot of the observed geometric mean radius and geometric standard deviation (denoted by '+') which satisfy the log-normal cloud droplets distribution during leg 3. The units for both the geometric mean radius and geometric standard deviation are in µm. Meanwhile, the contours of the extinction cross section (µ m^2) at 0.6 µm are also shown.

the value of extinction cross section is about 1.0×10^{-9} m^2, which does not fit our cloud droplet distribution data (Figure. 4.12).

Yet, it is found that the CCN (cloud condensation nuclei) concentration in the boundary layer was around 70 to 150 per cm^3 (Albrecht, personal communication). If we choose 75 per cm^3 and substitute into equation (4.11), the extinction cross section matches well with the cloud droplet spectrum observed. The cause of the discrepancy between the observed cloud droplet number density and the CCN number concentration may be that the FSSP does not measure all droplets.

From this procedure, $\overline{r_g}$= 9.5 μm and σ_g=1.4 μm are used to obtain the IR extinction cross section, IR asymmetry factor, and IR single scattering albedo. The values of these radiative properties are 900 μm^2, 0.93, and 0.68 respectively.

The 2-stream hemispheric mean scheme is then used to calculate the brightness temperature of these four types of clouds. The results are shown in Figure (4.13). Again, the geometry alone could not match the measured brightness temperature. However, when the extinction coefficient decrease linearly or quadratically from the cloud center to the cloud edge, the calculated brightness temperature are close to what is observed.

In our experiments 3 and 4, the extinction coefficient varies. However, the asymmetry factor and single scattering albedo were held constant. Even though that the asymmetry factor and single scattering albedo remain rather constant for common cloud droplet spectrum for visible radiation, the variation of the asymmetry factor and single scattering albedo in the IR is not negligible. By this, in our simulation, the cloud droplet distribution is assumed to be invariant in clouds, while the number density changes from cloud center to cloud edge. In fact, if we go back to Figure (3.3.2), it is clear that between 47 km to 39 km and between 32 km to 27 km of our arbitrary coordinate that the $\overline{r_g}$ and σ_g stay rather constant while number density increases from cloud edge to

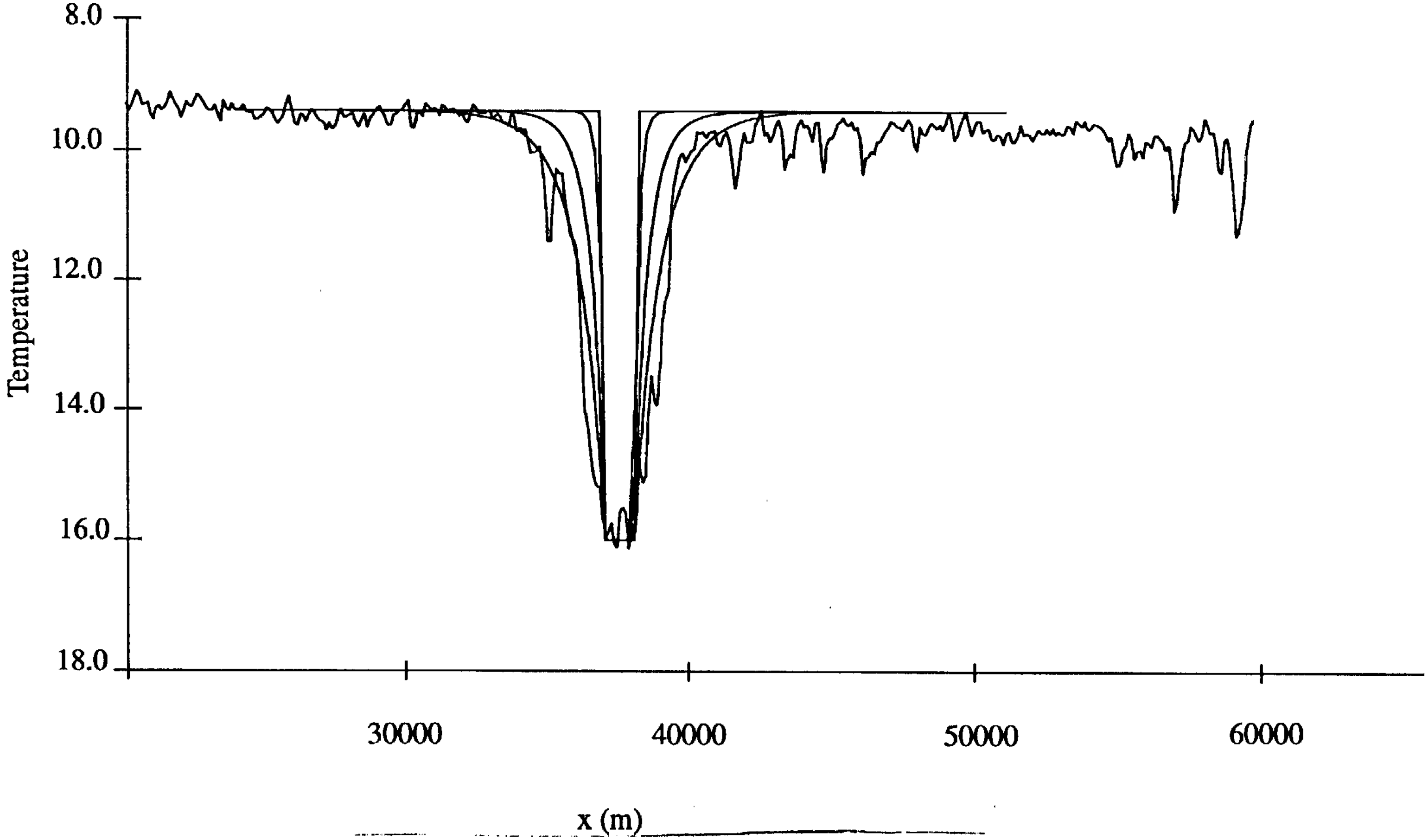

Figure (4.13) The observed brightness temperature and the brightness temperature for the four experiments (°C) along the flight path (20 km to 60 km). The observed brightness temperature has distinct small fluctuations; the other four lines are experiment 1, 2, 4 and 3 from the center of the hole inside out.

cloud center and decreases again near the cloud edge. However, because the time and space difference of leg 3 and leg 5, direct comparison is impossible.

One of the potential problem in these simple simulations is that the vertical variation of cloud microphysical properties is not considered. It is suggested that the vertical variation of cloud optical properties could be included and the effective particle radius of clouds (Nakajima and King, 1990) could also be applied in the further simulation of the radiation field of broken cloud field.

It should also be emphasized that, in this study, it is not the detailed quantities in which we are interested. But after analyzing of our results, we can conclude that for the case studied in these simulations, cloud geometry alone could not explain the drastic variation of reflectivity detected from the airplane, nor the brightness temperature variations.

Further studies of broken clouds would be valuable especially in collecting cloud microphysical data; for instance, mean radius, standard deviation and number density as a function of relative position in clouds. Therefore, a better understanding of stratocumulus clouds could be achieved, because these simulations infer the drastic differences of radiation field between plane-parallel clouds and its corresponding broken clouds in which the cloud optical properties change from cloud center to cloud edge.

Chapter 5

CONCLUSION

The Monte Carlo method was applied to simulate the visible radiation field over a broken cloud field. Four experiments have been conducted to reproduce the reflectivity and the brightness temperature measured in FIRE Electra flight 2 leg 5. One most significant feature in this flight is that the albedo varies almost linearly from 0.6 at cloud center to 0.05 at the holes between clouds, while the brightness temperature and the cloud top height remain unchanged through out the clouds.

The results suggest that the cloud geometry alone could not count for the change of albedo and the brightness temperature from cloud center to cloud edge. Both experiment 1 and 2, in which only the cloud shape effect is considered, fail to mimic the observed data. In contrast, both experiment 3 and 4, in which both the cloud effect and the variation of optical properties are considered, get consistent results with the measured data. It is the change of cloud optical properties inside the clouds more possible to be the main cause of what has been observed.

Assumptions and approximations in the simulations require further careful studies, especially for the building of a more accurate and fast way to generate free paths in a inhomogeneous medium.

In experiment 3 and 4, we vary the extinction coefficient linearly or quadratically from the cloud center the cloud edges. Because the extinction coefficient is a product of the cloud droplet number density and the volume extinction cross section, extra caution is needed to infer our results to the variation of microphysical properties inside the clouds.

In Section (3.2) we have demonstrated that the observed mean radius and its standard deviation in Flight 2 Leg 3 are rather constant in comparison to cloud droplet number density and LWC. Also, results of experiment 3 and 4, in which we assumed that the cloud droplet spectrum remained unchanged through out the cloud but only the cloud number density changed, are similar with the albedo and brightness temperature observed.

Conventionally, we think the cell structure of stratocumulus clouds is caused by the rising motion at cloud center and sinking motion at cloud edges. The cloud droplets will grow in the ascending air; however, when they reach the cloud top, they will mix with the entrained dry and warm air which are from the inversion above the cloud and start to evaporate and sink. The adiabatic warming in the descending motion will further contribute to the evaporation of cloud droplets. Smaller cloud droplets will soon vanish in the descending branch of vertical motion; meanwhile, a shift of cloud droplet spectrum toward larger cloud droplets is expected.

Yet, how does this argument link with the observed microphysical data and the simulation results? Why is the change of cloud droplet spectrum not observed? Why do we get good results when the change of cloud spectrum is not considered? Does that mean the shift of cloud droplet spectrum is small compared to the evaporation of smaller cloud droplets? More studies about the microphysical structure of stratocumulus clouds are needed to answer these questions.

It is also conjectured that whether the case studied here represents a typical case for stratocumulus clouds or not. First, the case we studied was at around solar noon, the cloud vertical side effect was actually at the minimum situation. Second, the horizontal scale of the breaks of the clouds is much smaller than that of clouds. Third, the clouds are approximately semi-infinite in geometry, because their horizontal scale (~25 km) overwhelms the effective width (~1 km) of the 2-D probability distribution of its homogeneous counterpart. Indeed, for those stratocumulus clouds that the fractional coverage of cloudy area is smaller and that the size of the cloud is comparable to the effective width of their 2-D probability distribution of reflected photons, the cloud geometry effect could be much more important. However, if this case is representative, not only the effect of cloud geometry but also the variation of cloud optical properties must be considered in the climate models.

References Cited

Albrecht, B., 1992: Personal Communication.

Blerkom, D. J., 1971: Diffuse Reflection From Clouds with Horizontal Inhomogeneities. *The Astrophysical Journal*, **166**, 235-242

Davies, R., 1978: The Effect of Finite Geometry on the Three-Dimensional Transfer of Solar Irradiance in Clouds. *Journal of the Atmospheric Science*, **35**, 1712-1725

Hale, G. M., and M. R. Querry, 1973: Optical Constants of Water in the 200-nm to 200μ m Wavelength Region. *Applied Optics*, **12**, 555-562

Kloesel, K. A., B. A. Albrecht and D. P. Wylie, 1988: *Fine Marine Stratocumulus Observations- Summary of Operations and Synoptic Conditions.* FIRE Technical Report No. 1 Available from Department of Meteorology, Pennsylvania Sate University, 16802

Kondratyev, K. Ya., 1969: *Radiation in the Atmosphere.* Academic Press, New York and London.

Lenoble, J., 1985: *Radiative Transfer in Scattering and Absorbing Atmospheres: Standard Computational Procedures.* **Vol. 1, 2**

Liou, K. N., 1980: *An Introduction to Atmospheric Radiation.* Academic Press, New York

Mckee, T. B., and S. K. Cox, 1974: Scattering of Visible Radiation by Finite Clouds. *Journal of the Atmospheric Science*, **31**, 1885-1892

Nakajima, T., and M. D. King, 1990: Determination of the Optical Thickness and Effective Particle Radius of Clouds from Reflected Solar Radiation Measurement. Part I: Theory. *Journal of the Atmospheric Science*, **47**, 1878-1893

Ramanathan, V., R. D. Cess, E. F. Harrison, P. Minnis, B. R. Barkstrom, E. Ahmad, D. Hartmann, 1989: Cloud-Radiative Forcing and Climate: Results from the Earth Radiation Budget Experiment. *Science*, **243**, 57-63

Spencer, J. W., 1971: Fourier Representation of the Position of the Sun. *Search*, **2**, 172

Toon, O. B., C. P. Mckay, T. P. Ackerman, and K. Santhanam, 1989: Rapid Calculation of Radiative Heating Rates and Photodissociation Rates in Inhomogeneous Multiple Scattering Atmosphere. *Journal of Geophysical Research,* **94**, No. D13, 16,287-16,301

Welch, R. M. and B. A. Wielicki, 1984: Stratocumulus Cloud Field Reflected fluxes: The Effect of Cloud Shape. *Journal of the Atmospheric Science,* **41**, 3085-3103

Zuev, V. E., T. B. Zhuravleva and G. A. Titov, 1987: Modeling of Outgoing Long-Wave Radiation in the Presence of Broken Clouds. *Journal of Geophysical Research,* **92**, No. D5, 5533-5539

Additional References

Marchuk, G. I., G. A. Mikhailov, M. A. Nazaraliev, R. A. Darbinjan, B. A. Kargin and B. S. Elepov, 1979: *The Monte Carlo Methods in Atmospheric Optics.* Springer-Verlog, New York.

Paltridge, G. W. and C. M. R. Platt, 1976: *Radiative Process in Meteorology and Climatology.* Elsevier Scientific Pub. Co., New York.

Walpole, R. E. and R. H. Myers, 1989: *Probability and Statistics for Engineers and Scientists. Fourth Edition.* Macmillan Publishing Company, New York.